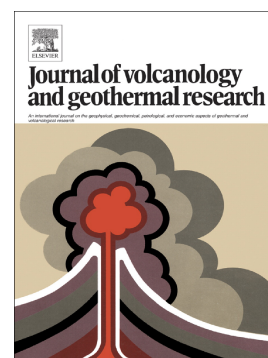


Journal Pre-proof

What can Olympus Mons tell us about the Martian lithosphere?

Nicola C. Taylor, Jessica H. Johnson, Richard A. Herd, Catherine E. Regan



PII: S0377-0273(20)30252-3

DOI: <https://doi.org/10.1016/j.jvolgeores.2020.106981>

Reference: VOLGEO 106981

To appear in: *Journal of Volcanology and Geothermal Research*

Received date: 5 May 2020

Revised date: 15 June 2020

Accepted date: 16 June 2020

Please cite this article as: N.C. Taylor, J.H. Johnson, R.A. Herd, et al., What can Olympus Mons tell us about the Martian lithosphere?, *Journal of Volcanology and Geothermal Research* (2020), <https://doi.org/10.1016/j.jvolgeores.2020.106981>

This is a PDF file of an article that has undergone enhancements after acceptance, such as the addition of a cover page and metadata, and formatting for readability, but it is not yet the definitive version of record. This version will undergo additional copyediting, typesetting and review before it is published in its final form, but we are providing this version to give early visibility of the article. Please note that, during the production process, errors may be discovered which could affect the content, and all legal disclaimers that apply to the journal pertain.

© 2020 Published by Elsevier.

What can Olympus Mons tell us about the Martian lithosphere?

Nicola C. Taylor^{a,*}, Jessica H. Johnson^a, Richard A. Herd^a, Catherine E. Regan^b

^a*School of Environmental Sciences, University of East Anglia, Norwich, UK*

^b*School of Physics and Astronomy, University College London, UK*

*Corresponding author

Email address: Nicola.C.Taylor@uea.ac.uk (Nicola C. Taylor)

Abstract

Under gravitational loading, a volcanic edifice deforms, and the underlying lithosphere downflexes. This has been observed on Earth, but is equally true on other planets. We use finite element models to simulate this gravity-driven deformation at Olympus Mons on Mars. Eleven model parameters, including the geometry and material properties of the edifice, lithosphere and underlying asthenosphere, are varied to establish which parameters have the greatest effect on deformation. Values for parameters that affect deformation at Olympus Mons, Mars, are constrained by minimizing misfit between modeled and observed measurements of edifice height, edifice radius, and flexural moat width. Our inferred value for the Young's modulus of the Martian lithosphere, 17.8 GPa, is significantly lower than values used previously, suggesting that the Martian lithosphere is more porous than generally assumed. The best-fitting values for other parameters: edifice density (2111–2389 kg.m⁻³) and lithosphere thickness (83.3 km) are within ranges proposed hitherto. The best-fitting values of model parameters are interdependent; a decrease in lithosphere Young's modulus must be accompanied by a decrease in edifice density and/or an increase in lithosphere thickness. Our results identify the parameters that should be considered within all models of gravity-driven volcano deformation; highlight the importance of the often-overlooked Young's modulus; and provide further constraints on the properties of the Martian lithosphere, namely its porosity, which have implications for the transport and storage of fluid throughout Mars' history.

Highlights

- We use FEA to constrain physical properties of Olympus Mons and Mars' lithosphere
- We constrain the Young's modulus of the Martian lithosphere for the first time
- Mars' lithosphere is less stiff and may be more porous than was previously assumed

Keywords: Lithospheric flexure, Finite element models, Olympus Mons, Mars

1. Introduction

Gravitational loading from a volcanic edifice causes the underlying lithosphere to downflex. This lithospheric flexure is affected by the properties and geometry of the volcanic edifice, lithosphere and underlying asthenosphere (e.g. Beuthe et al., 2012; Isherwood et al., 2013; Musiol et al., 2016). On Earth, lithospheric flexure can be modeled, but also observed within seismic reflection surveys (e.g. Watts et al., 1985), and inferred from elevated coral deposits (e.g.

Grigg and Jones, 1997). On other planets, ground-collected data are limited, so topographic and gravity data are principally used to interpret lithospheric flexure.

Olympus Mons, Mars, provides an interesting paradigm for studying lithospheric flexure because of its immense size. Tectonic plate movement on Mars possibly never started (O'Rourke and Korenaga, 2012; Leone, 2017), or ceased early in the planet's history (Frey et al., 2002). This enabled Olympus Mons to grow to dimensions that dwarf volcanoes on Earth, and has preserved an extensive history of volcanic activity. Previous studies have used a range of techniques, including analog, analytical and numerical modeling (e.g. Byrne et al., 2013; Musiol et al., 2016), geochemical analyses of meteorite samples (e.g. Baratoux et al., 2014), crater counting (e.g. Isherwood et al., 2013), and gravitational admittance surveys (e.g. Dorman and Lewis, 1970; Watts, 2001) to provide constraints on values for properties that affect lithospheric flexure at Olympus Mons.

To construct a model of lithospheric flexure, values must be assigned to a range of model parameters. These include the model geometry (dimensions of the edifice and lithosphere), material properties of model components (density, Young's modulus and Poisson's ratio of the edifice and lithosphere), and the conditions at boundaries between model components (coefficient of friction between edifice and lithosphere). On Mars, there are significant uncertainties associated with values for some of these parameters because they cannot be measured directly. In addition, simulating lithospheric flexure is often a non-unique problem; the same flexure can be produced by different combinations of values of model parameters. For example, there is a trade-off between lithospheric thickness and edifice density (e.g. Beuthe et al., 2012); if lithospheric thickness is increased, edifice density must also increase to produce the same deformation (when other model parameters remain constant). We suggest that similar trade-offs exist between other model parameters, but the effects that some model parameters have on lithospheric flexure have not been quantified, so these trade-offs have not been studied. Thus, values that define the characteristics of volcanoes and the subsurface they overlie may differ when parameter values are better defined, and when the effects that all model parameters have on deformation are better quantified.

Here, finite element modeling is used to evaluate which model parameters have the greatest effect on lithospheric flexure. We extend previous work by considering the effects of a greater number of model parameters. The parameters that have the greatest effect on deformation are then simultaneously varied. By comparing modelled lithospheric flexure to observed topography at Olympus Mons, we place bounds on values for parameters that define the edifice, lithosphere and asthenosphere at Olympus Mons. A better understanding of the parameters that affect lithospheric flexure is of benefit for a range of geodetic studies. Constraining values of parameters that define lithospheric flexure at Olympus Mons is useful for understanding this volcano and interpreting phenomena on Mars, as well as for understanding the behavior of large volcanoes elsewhere, including on Earth.

2. Olympus Mons

Olympus Mons lies in Mars' northern hemisphere (226.0° E, 16.5° N), on the northwestern flank of the Tharsis rise, a vast ($30 \times 10^6 \text{ km}^2$) volcanic province that covers approximately one-quarter of Mars' surface (Figure 1, Kiefer, 2003; Hynek et al., 2011; Isherwood et al., 2013). The extensive igneous activity at Tharsis is attributed to migration of mantle plumes under the lithosphere (Leone, 2016), or to decompression melting of mantle plumes upwelling from the core-mantle boundary (Wenzel, 2004; Zhong, 2009; Hynek et al., 2011; Kiefer and Li, 2016). The

Tharsis region was predominantly emplaced between 4.0 and 3.7 Ga (Phillips, 2001; Williams et al., 2008). Crater-counting suggests that smaller-scale volcanism may have occurred within the last 2 Myr (Neukum et al., 2004; Schumacher and Breuer, 2007), but this conflicts with results from thermal models that suggest volcanism on Mars ceased in the Hesperian (at least 3.5 Ga, Hauck, 2002; Grott et al., 2005; Leone et al., 2014; Leone, 2017).

Olympus Mons is the largest known volcano in the solar system. The volcano's edifice has a total exposed volume of $2.4 \times 10^{15} \text{ m}^3$, a basal radius of around 300 km, and rises to an elevation 22 km above the surrounding plains (Plescia, 2004). Crater counting and flexural modeling suggest that the majority of the edifice was formed between $3.67_{-0.10}^{+0.05}$ and $2.54_{-0.69}^{+0.55}$ Ga (Isherwood et al., 2013). However, the nested calderas at the summit of Olympus Mons provide evidence for later volcanic activity (Neukum et al., 2004; Robbins et al., 2011), and these later magmatic events may have also contributed to edifice construction (Chadwick et al., 2015).

The gravity-driven deformation processes of volcano sagging and spreading (Figure 2) have occurred contemporaneously to shape Olympus Mons. Volcanic sagging occurs when the weight of the edifice causes the underlying lithosphere to downflex. The edifice may be coupled to the lithosphere, having an end-member sagging architecture, or be decoupled from the lithosphere, with a hybrid sagging-spreading architecture. Olympus Mons is in the latter category (Byrne et al., 2013). Features that indicate volcanic sagging has occurred at Olympus Mons include flank terraces, and a flexural bulge and flexural moat that encircle the volcano. The flexural moat is filled with landslide deposits and lava flows (Weller et al., 2014; McGovern et al., 2015; Chadwick et al., 2015). Gravity-driven volcano spreading acts when the edifice and lithosphere are decoupled. A volcano with an end-member spreading architecture will collapse outwards along its basal décollement without deforming the lithosphere (Borgia et al., 2000), whereas volcanoes elsewhere on the sagging-spreading continuum (e.g. Olympus Mons) collapse outwards along their basal décollements but also deform the lithosphere. Gravity-driven spreading at Olympus Mons has led to the formation of leaf grabens and the Olympus Mons basal scarp - a steep escarpment up to 10 km high that surrounds the majority of the edifice (McGovern and Morgan, 2009; Weller et al., 2014).

2.1. Topography

Topographic analyses were used to quantify the current dimensions of Olympus Mons' edifice and encircling flexural bulge (due to gravity-driven volcanic sagging). These values were subsequently used to evaluate model results (Section 5.2). The Mars Orbiter Laser Altimeter (MOLA) has collected observations of Martian topography at resolutions of around 500 by 1 m (horizontal by vertical, Smith, 1999; Smith et al., 2001). Using MOLA data within JMars, a planetary GIS (Christensen et al., 2009), we plot eight 1500 km-long radial topographic profiles from the centre of Olympus Mons (profile locations shown on Figure 1). Olympus Mons is located on the northwest flank of the Tharsis rise, and consequently the topographic surface under Olympus Mons is at higher elevation to the southeast than to the northwest (Phillips, 2001). To account for this topographic heterogeneity, each topographic profile was adjusted to a reference 0 m elevation, defined as the elevation of infill at the base of the edifice. The change in gradient was used to define the boundary between edifice and infill (the first distance where the gradient, averaged over 36 km, was < 0.001). In making this adjustment, two simplifying assumptions were made: the fill level in the flexural moat is uniform around the edifice, and the elevation of infill is lower than the flexural bulge. The symmetry of Olympus Mons' edifice (Figure 1)

provides justification for the first assumption. This symmetry suggests that volcanism, and thus the volume of volcanic deposits within the flexural moat, is relatively constant radially. However, to make a more realistic estimate of moat infill, additional modeling would be required to quantify the topographic gradient that underlies Olympus Mons. This modeling is beyond the scope of the paper. Our second assumption is justified using topographic maps. For most of the topographic profiles (Figures 1 and 3), the flexural bulge, associated with a positive change in topography, can be observed. In addition, topographic analyses of the latest lava flows at Olympus Mons suggest that lava has flowed away from the edifice, but has not crossed the flexural bulge (Chadwick et al., 2015). Without additional geophysical data, for example from seismic reflection surveys, we cannot confirm how the depth of infill relates to the flexural bulge, as we can on Earth (e.g. Watts et al., 1985).

For each topographic profile (Figure 3), in conjunction with elevation maps (Figure 1), edifice height, edifice radius, and the width of the flexural moat were measured. For the west and northwest profiles, the edge of the flexural moat was unclear, so this parameter was not measured. The means and standard deviations of edifice height (\hat{x}_h), edifice radius (\hat{x}_r), and the width of the flexural moat (\hat{x}_m) were calculated; $\hat{x}_h = 21.2 \pm 1.1$ km, $\hat{x}_r = 357 \pm 35$ km and $\hat{x}_m = 331 \pm 108$ km (mean \pm standard deviation).

3. Model setup

3.1. Geometric setup

COMSOL Multiphysics (v5.4) was used for all finite element modeling. Our models had a simple two-dimensional axisymmetric model geometry. This simplification was justified by the symmetry of Olympus Mons' edifice. Our models represented the dynamic structure of the outer planetary layers (e.g. Breuer and Spohn, 2006), comprising a volcanic edifice and lithosphere and incorporating the effects of buoyancy from the asthenosphere as a boundary force (Figure 4). We did not distinguish between crustal and mantle lithosphere; we modeled flexure of a single, homogeneous, elastic layer, which we termed the lithosphere. Although this approach limits our conclusions about properties of the lithosphere, values that define crustal thickness and density at regional scales have been poorly constrained on Mars (e.g. Beuthe et al., 2012). Introducing these additional complexities, and the corresponding additional degrees of freedom, into our models was therefore not justified.

The model geometry extended to 3000 km in the radial direction to reduce boundary effects. The outside vertical boundary was free to move vertically, but fixed radially - a roller boundary. There was a frictional interface between the edifice and lithosphere. The mesh for the volcanic edifice and lithosphere comprised triangular elements. The elements in the edifice mesh had a minimum dimension of 225 m and a maximum dimension of 3000 m, and the mesh elements in the lithosphere had a minimum dimension of 225 m and a maximum dimension of 60,000 m (Table S1, Figure S1). Sensitivity tests were performed to ensure that the element size did not affect the model results.

3.2. Rheology

We represented the edifice and lithosphere as solid elastic bodies. The majority of

Olympus Mons' edifice had been emplaced by 2.54 Ga, and subsequent rates of magma generation have been non-existent, or too low to sustain an active magma reservoir (Wilson et al., 2001; Isherwood et al., 2013). We therefore assumed that much of the edifice and lithosphere are cooler than the brittle-ductile interface, and thus respond elastically to applied stress (Del Negro et al., 2009).

In comparison to the overlying lithosphere, the asthenosphere is weak and behaves as a fluid over geological time. The effects of buoyancy from a viscous fluid asthenosphere were incorporated in our models as a boundary force. Incorporating a more realistic asthenosphere would require further assumptions to be made about the currently poorly-described Martian mantle (e.g. Breuer and Spohn, 2006).

3.3. Volcanic loading

Gravitational loading was applied as a body force to the edifice with gravitational field strength 3.71 m.s^{-2} . Previous work by Musiol et al. (2016) demonstrated that surface faults at Olympus Mons can be formed under both instantaneous loading and growing load scenarios. We modeled a growing load scenario, and found that deformation modeled from growing and instantaneous loading scenarios converged within 2.54 Gyr (the estimated age of the majority of the edifice, (Isherwood et al., 2013). Figure S2 displays these results. Thus, in all models we used an instantaneous loading scenario for the edifice, which decreases computation time.

4. Model variables

We tested the sensitivity of models of lithospheric flexure to eleven model parameters: asthenosphere density, lithosphere thickness, lithosphere density, lithosphere Poisson's ratio, lithosphere Young's modulus, initial edifice height, initial edifice radius, edifice density, edifice Poisson's ratio, edifice Young's modulus, and the frictional coefficient between the edifice and the lithosphere. Table 1 summarizes the tested values for all model parameters.

4.1. Asthenosphere density

Values that define the density of the Martian mantle have been obtained using geophysical and geochemical techniques. The moment-of-inertia factor has been used to estimate average densities of the Martian mantle, with results ranging from 3330 to 3740 kg.m^{-3} (e.g. Johnston et al., 1974; Johnston and Toksöz, 1977; Okal and Anderson, 1978). Goettel (1981) constrained mantle density to $3440 \pm 60 \text{ kg.m}^{-3}$ by using analytical models with a range of density distributions. This result has subsequently been used within many models of lithospheric flexure (e.g. McGovern et al., 2002; Belleguic et al., 2005; Beuthe et al., 2012; Musiol et al., 2016). The differences in inferred mantle density are attributed to uncertainty in crustal density and thickness (e.g. Bertka and Fei, 1998) and uncertainty in Mars' precession rate, which affects the moment-of-inertia factor (e.g. Folkner et al., 1997; Yoder and Standish, 1997). Geochemical analyses of meteorites (e.g. Dreibus and Wanke, 1985), and experiments undertaken at high temperatures and pressures (Bertka and Fei, 1997; Bertka and Fei, 1998) have also been used to infer the density of the Martian mantle. These results align with those derived from moment-of-inertia models, and are also affected by the thickness and density of the crust. Here we

varied asthenosphere density between 3300 and 3600 kg.m^{-3} . We did not consider the highest values of asthenosphere density inferred from previous studies because our models only represent the outer region of the mantle, which has a lower density than the mantle at greater depths (e.g. Bertka and Fei, 1998).

4.2. Lithosphere variables

4.2.1. Lithosphere thickness

Lithosphere thickness has been estimated using analytical models and gravitational admittance. Analytical thin-plate models (where a thin elastic plate overlies a viscous fluid, e.g. Brochie and Silvester, 1969), placed a lower bound of 150 km for lithosphere thickness at Olympus Mons (Comer et al., 1985). An analytical thin-shell model (Isherwood et al., 2013) favored lithosphere thicknesses between 70 and 80 km, but a unique value of thickness could not be determined. Gravitational admittance surveys have used topography and gravity data from spacecraft Mars Global Surveyor (MGS) and Viking 2 to estimate that lithosphere thickness in the Tharsis province is approximately 70 km (McKenzie et al., 2002), and this value increases to > 70 km (McGovern et al., 2002, 2004) or to 93 ± 40 km (Belleguic et al., 2005) at Olympus Mons. The inherent trade-off between lithosphere thickness and relatively unconstrained parameters, including crustal and lithospheric densities and the amount of bottom loading, limits the constraints that can be placed on values of lithosphere thickness at Olympus Mons, despite the increasing resolution of geodetic data (Beuthe et al., 2012). Here we evaluated lithospheric flexure for lithosphere thicknesses between 40 and 170 km.

4.2.2. Lithosphere density

The density of crustal lithosphere is less than the density of mantle lithosphere. However, our models comprise a single lithosphere layer (Section 3.1), so our range of evaluated values for lithosphere density includes densities computed for crustal and mantle lithosphere. Estimates of crustal densities have been made using geochemical and geophysical techniques, and we discuss values for asthenosphere density previously (Section 4.1).

An average crustal density of 3100 kg.m^{-3} is compatible with the major element chemistry of Martian meteorites and surface element concentrations (Baratoux et al., 2014). However, this density requires a thick crustal layer (>100 km), which some studies have suggested is incompatible with results from gravitational admittance (Pauer and Breuer, 2008; Baratoux et al., 2014). Gravitational admittance analyses have suggested that average crustal density is $2582 \pm 95 \text{ kg.m}^{-3}$, which increases to $3231 \pm 95 \text{ kg.m}^{-3}$ in the Tharsis province (Goossens et al., 2017). Variation in crustal density with depth is also hypothesised, but the parameters for this depth-dependence cannot yet be confidently determined (Goossens et al., 2017). 2900 kg.m^{-3} is considered an average value for crustal density on Mars, and is often used for modeling (e.g. Neumann, 2004; Musiol et al., 2016). We varied lithosphere density between 2500 and 3500 kg.m^{-3} , a range that encompasses results of many previous studies for crustal lithosphere, and extends to typical densities assumed for the mantle lithosphere.

4.2.3. Lithosphere Poisson's ratio

The Poisson effect, the tendency of an elastic material to expand or contract perpendicularly to the direction of loading, is quantified by the ratio of transverse strain to axial strain, Poisson's ratio (e.g. Gercek, 2007). Martian meteorite samples, from which Poisson's ratio can be determined experimentally, are limited, so numerical modeling has been used to estimate values for the Olympus Mons region. Dimitrova and Haines (2013) used numerical models to show that the state of stress, and hence faulting, observed on Mars could be best explained when the Poisson's ratio of the lithosphere was 0.5 (an incompressible lithosphere). However, many models of lithospheric flexure at Martian volcanoes assign Poisson's ratio values of 0.25–0.30 to the lithosphere (e.g. McGovern and Solomon, 1993; McGovern et al., 2002; Belleguic et al., 2005; Beuthe et al., 2012; Isherwood et al., 2013), and these values align with the experimentally-derived values of Poisson's ratio for Earth's oceanic crust ($\nu = 0.25$, Collier and Singh, 1998). To incorporate values for lithosphere Poisson's ratio found by, and used within, previous studies, we varied this parameter between 0.1 and 0.49 (convergence of finite element models is impossible when Poisson's ratio is equal to 0.5, e.g. Kwon et al., 2014).

4.2.4. Lithosphere Young's modulus

Young's modulus reports the ratio of stress to strain in the linear elasticity regime of uniaxial deformation; it describes a material's stiffness. Values that define the Young's modulus for Martian rocks are rarely discussed, thus our range of tested values is informed by laboratory testing of terrestrial basalts. We assume that the Martian lithosphere is basaltic (e.g. McSween et al., 2009), and thus has elastic properties analogous to terrestrial basalt. Heap et al. (2020) reviewed the Young's moduli of terrestrial volcanic rocks, and found that a value of 5.4 GPa is an average value. Although the methodology used in this study is for shallow lithologies, and Young's modulus will increase with depth (due to decreasing porosity and compositional changes, (Tesauro et al., 2012), this value provides a lower bound on potential values for lithosphere Young's modulus. In addition, Mars has a lower surface gravity than Earth, which means that the Martian lithosphere is more fractured, more porous and weaker, and consequently has a lower Young's modulus (Heap et al. 2017, 2020). However, previous studies have typically assigned values between 100 and 120 GPa to the Young's modulus of crustal and asthenospheric lithosphere on Mars (e.g. McGovern et al., 2002; Belleguic et al., 2005; Beuthe et al., 2012; Isherwood et al., 2013; Musiol et al., 2016). To incorporate the results of Heap et al. (2020), in addition to evaluating the values used in previous studies, we considered a wide range of values for lithosphere Young's modulus: 5 to 120 GPa.

4.3. Edifice variables

4.3.1. Edifice geometry

In our models, forcing comes from gravity that is applied as a body load to the edifice (Figure 4a). Under this applied force, the lithosphere downflexes and the edifice deforms (Figure 4b). Consequently, the minimum value of initial edifice height tested in our models was equal to \hat{x}_h , 21 km, the current height of Olympus Mons' edifice (because the edifice can only decrease in height under gravitational loading). The maximum tested value of initial edifice height was 45 km. However, unlike edifice height, the radius of the edifice can increase or decrease during gravitational loading depending on amount of gravitational sagging and spreading (Figure 2), and

the values of other model variables. Thus, the mean value of initial edifice radius that we tested was equal to \hat{x}_r (360 km), the current radius of Olympus Mons' edifice (Section 2.1). The range of tested values for initial edifice radius was 150 to 570 km. The values that we define for initial edifice height and radius are used to construct our initial model geometry, and do not incorporate the true incremental growth of the edifice (because we use an instantaneous loading scenario, Section 3.3). Thus, the best-fitting values for initial edifice height and radius determined within our modeling will provide a measure of the overall volume of the edifice (including that which is below 0 m elevation) at present.

4.3.2. Edifice density

Gravity and topography measurements from MGS were used by McGovern et al. (2002, 2004) to estimate that the density of Olympus Mons' edifice was 3150 kg.m^{-3} . This result was increased to $3252 \pm 150 \text{ kg.m}^{-3}$ by Belleguic et al. (2005). Subsequent spacecraft Mars Express and Mars Reconnaissance collected higher-resolution gravity data at Olympus Mons, but these data could not place additional constraints on edifice density (Beuthe et al., 2012). Ganesh et al. (2020) used data collected by the SHallow RADar (SHARAD) instrument onboard the Mars Reconnaissance Orbiter, to estimate the density of Arsia Mons' edifice (8° S , 120° W , Figure 1). The resulting densities for deposits in the upper layers of Arsia Mons' caldera were between 1800 kg.m^{-3} and 3120 kg.m^{-3} . Martian density estimates cannot be verified against erupted samples, so we use results from laboratory testing of Hawaiian basalt to place additional bounds on the probable density range at Olympus Mons. The average density of highly-vesicular fall deposits at Kīlauea volcano was $203\text{--}1421 \text{ kg.m}^{-3}$ (Houghton and Wilson, 1989), and samples from a 3.097 km-deep borehole at Mauna Loa volcano had average density around 2550 kg.m^{-3} (Moore, 2001). We varied edifice density between 1000 and 3500 kg.m^{-3} . This range excludes the highest-vesicularity fall deposits sampled at Hawai'i, because these samples have densities that are unrealistically low for an average value for Olympus Mons' edifice. The maximum tested value of edifice density is the maximum tested value of lithosphere density.

4.3.3. Edifice Poisson's ratio

As for the Martian lithosphere, there has been little analysis of Poisson's ratio for volcanic edifices on Mars. We tested the same range of values for edifice Poisson's ratio as we did for lithosphere Poisson's ratio: 0.1 - 0.49. We assume that volcanism at Olympus Mons is basaltic (e.g. Chadwick et al., 2015; Crown and Ramsey, 2017), and a typical range of values for Poisson's ratio for basalt is 0.1 to 0.35 (Gercek, 2007). Near-surface terrestrial volcanic rock masses with average porosity also have Poisson's ratios in this range - typically between 0.25 and 0.35 (Heap et al., 2020). Our tested range includes values of Poisson's ratio assigned to edifices within previous models of lithospheric flexure at Olympus Mons (e.g. McGovern et al., 2002; Belleguic et al., 2005; Isherwood et al., 2013; Musiol et al., 2016), and extends to the value of lithosphere Poisson's ratio that Dimitrova and Haines (2013) suggested could best explained observed faulting on Mars (Section 4.2.3).

4.3.4. Edifice Young's modulus

The Young's modulus of the Olympus Mons edifice has been poorly constrained. However, again using the assumption that Martian volcanism is basaltic (e.g. Chadwick et al., 2015; Crown and Ramsey, 2017), we consider experimentally-derived values for Young's modulus from terrestrial basalt. The minimum tested value of edifice Young's modulus, 5 GPa, is based on a result from Heap et al. (2020). This value is calculated for shallow terrestrial lithologies. However, the combination of lower surface gravity on Mars (which will cause a reduction in Young's modulus, e.g. Heap et al., 2017), and the large size of Olympus Mons' edifice (so the Young's modulus of the edifice will be significantly greater at its base than at its surface), means that 5 GPa is an appropriate lower limit for edifice Young's modulus. Previous models of flexure at Olympus Mons (e.g. Musiol et al., 2016), assigned values much greater than 5 GPa to edifice Young's modulus. We therefore evaluated a wide range of values for edifice Young's modulus, 5–85 GPa, to incorporate values used in previous studies, but we anticipate that values at the upper end of this range may be unrealistically large, following the review by Heap et al. (2020).

4.4. Friction

The coefficient of friction between the edifice and lithosphere controls the morphology of the edifice (Section 2, Byrne et al., 2013). The morphology of Olympus Mons suggests that the edifice has spread along its basal décollement, justifying the addition of friction to our models. Musiol et al. (2016) suggested that the coefficient of friction between Olympus Mons' edifice and lithosphere could be as low as 0.1. However, when lithospheric flexure was modeled at Hawai'i (Zhong and Watts, 2013), the best-fitting frictional coefficient was between 0.25 and 0.70. At Hawai'i, the basal décollement lies between the volcanic edifice and oceanic crust, with wet oceanic sediments lubricating the interface (Denlinger and Morgan, 2014), thus the frictional coefficient at Hawai'i is predicted to be less than at Olympus Mons. Given the ambiguity about the frictional coefficient, we tested values between 0.1 and 0.9.

5. Results

5.1. Independently varying parameters

We first established which model parameters had the greatest effect on lithospheric flexure. The eleven model parameters (asthenosphere density, lithosphere thickness, lithosphere density, lithosphere Poisson's ratio, lithosphere Young's modulus, initial edifice height, initial edifice radius, edifice density, edifice Poisson's ratio, edifice Young's modulus, and the frictional coefficient between the edifice and the lithosphere) under investigation were varied independently. Ten evenly-spread values for each variable were tested (110 models altogether). For each model, lithospheric flexure was measured in three ways: post-loading edifice height, x_h , post-loading edifice radius, x_r , and the width of the flexural moat, x_m .

For each tested model parameter, we computed the percentage difference in x_h (dx_h), x_r (dx_r) and x_m (dx_m) across the range of tested parameter values:

$$dx_{h,r,m} = 100 \times \frac{\max(x_{h,r,m}) - \min(x_{h,r,m})}{0.5(\max(x_{h,r,m}) + \min(x_{h,r,m}))} \quad (1)$$

The eleven values of dx_h , dx_r and dx_m (one for each tested model parameter) were ranked in descending order from 11 to 1 (Figure 5a - c). The parameter with the largest dx_h , and thus greatest effect on x_h , was ranked 11 (the same procedure was followed for dx_r and dx_m). An average rank was assigned if multiple parameters had equal dx_h , dx_r or dx_m . The ranks for dx_h , dx_r and dx_m were then summed (Figure 5d) to establish which parameters had the greatest effect on overall lithospheric flexure.

Both model geometry (initial edifice height, initial edifice radius, lithosphere thickness) and material properties (density, Young's Modulus, Poisson's ratio) affected lithospheric flexure (Figure 5). All interrogated model parameters had an effect on x_h . However, only ten of the parameters affected x_r and only five affected x_m . Overall, initial edifice radius had the most effect on lithospheric flexure, and lithosphere density had the least. The measure of lithospheric flexure dictated which model variable was most influential. As expected, the initial edifice geometry had the greatest effect on the final edifice geometry (initial edifice height had the greatest effect on x_h , and initial edifice radius had the greatest effect on x_r). Lithosphere thickness had the greatest effect on x_m . Model variables generally ranked in a similar order regardless of the measure of lithospheric flexure evaluated, but there were some exceptions. For example, initial edifice height had the greatest effect on x_h , but had little effect on x_r and x_m . Similarly, lithosphere Poisson's ratio had the 5th highest rank for its effect on x_m , but little effect on x_h and no effect on x_r .

5.2. Constraining model parameters

We simultaneously varied the five model parameters that our previous analyses (Section 5.1) suggested had the greatest effect on deformation: initial edifice radius, edifice density, lithosphere thickness, lithosphere Young's modulus and asthenosphere density. Values for five of the six remaining parameters were fixed at the control values defined in Table 1. The coefficient of friction was reduced to zero, because it had little effect on lithospheric flexure (Figure 5) and by doing this the frictional interface could be replaced by a welded contact, which improved the convergence of our models. Ten values of each parameter were tested; number of models, $n = 100,000$. As before, modeled lithospheric flexure was quantified by the final edifice height and radius, x_h and x_r respectively, and the width of the flexural moat, x_m . Modeled x_h , x_r and x_m were compared to the mean values of Olympus Mons' current edifice height (\hat{x}_h), radius (\hat{x}_r), and flexural moat width (\hat{x}_m , Figure 3). For each model ($i = 1$ to $i = n$), we computed the residual for each measure of lithospheric flexure. e_h , e_r and e_m are defined as the residuals associated with edifice height, edifice radius, and flexural moat width respectively.

$$e_{(h,r,m)i} = |x_{(h,r,m)i} - \hat{x}_{(h,r,m)i}| \quad (2)$$

Residuals were normalized between 0 (no residual) and 1 (largest residual):

$$\tilde{e}_{(h,r,m)i} = \frac{e_{(h,r,m)i}}{\max\{e_{(h,r,m)(i=1)}, \dots, e_{(h,r,m)(i=n)}\}} \quad (3)$$

We define the overall residual for each model, \tilde{e} :

$$\tilde{e}_i = \tilde{e}_{hi} + \tilde{e}_{ri} + \tilde{e}_{mi} \quad (4)$$

Figure 6 displays the overall residuals, \tilde{e} , for each tested value for each of the five interrogated model parameters and Figure 7 displays the three residuals, \tilde{e}_h , \tilde{e}_r and \tilde{e}_m separately. Kruskal-Wallis and post-hoc Dunn's tests were used to test for differences in \tilde{e} , \tilde{e}_h , \tilde{e}_r and \tilde{e}_m . For all results, $n=10,000$ and we set a 95% confidence limit. All quoted p -values have been adjusted for multiple comparisons using a Bonferroni correction. The results of all statistical tests are presented in Table S3.

We used \tilde{e} to estimate the best-fitting values of initial edifice radius, edifice density, lithosphere thickness and lithosphere Young's modulus at Olympus Mons (Figure 6, Table S2). We cannot estimate a value for asthenosphere density because there were no significant differences in \tilde{e} between all tested values. The best-fitting value of initial edifice radius was 383 km, and \tilde{e} for this value was smaller than \tilde{e} for all other tested values ($p < 0.0001$ for all tests). However, we cannot use \tilde{e} to determine a unique value for edifice density, lithosphere thickness or lithosphere Young's modulus because there was not a significant difference between the minimum \tilde{e} and other \tilde{e} for these parameters. For example, the best-fitting value of edifice density was 2389 kg.m⁻³, but \tilde{e} for this value was not significantly different from \tilde{e} when edifice density was 1833, 2111 and 2667 kg.m⁻³ ($p = 0.19-1.0$).

The best-fitting values for four out of the five model parameters were affected by the measure of lithospheric flexure that was evaluated (Figure 7, Table S2). For initial edifice radius, all three measures of lithospheric flexure suggested that a best-fitting value was 383 km. When \tilde{e}_r were compared, 383 km was the uniquely best-fitting value, whereas when \tilde{e}_h and \tilde{e}_m were evaluated, 383 km lay within a range of best-fitting values. However, the best-fitting values for edifice density, lithosphere thickness and lithosphere Young's modulus were significantly different depending on whether \tilde{e}_h , \tilde{e}_r or \tilde{e}_m were analyzed.

In addition, the three measures of lithospheric flexure placed the tightest constraints on different model parameters (Figure 7, Table S2). Comparing x_h and \hat{x}_h (residual \tilde{e}_h), provided the tightest constraints on the values of edifice density (2111–2389 km) and lithosphere Young's modulus (17.8–30.6 GPa), but suggested a wider range of best-fitting values for initial edifice radius and lithosphere thickness. Comparing x_r and \hat{x}_r (residual \tilde{e}_r), provided a unique best-fitting value for initial edifice radius (383 km), but for all other parameters there were at least five best-fitting values. Likewise, when x_m and \hat{x}_m were considered (residual \tilde{e}_m), the

best-fitting value for lithosphere thickness was unique (83.3 km), but a range of values for initial edifice radius, edifice density and lithosphere Young's modulus had non-different \tilde{e}_m . Table 2 summarizes the best-fitting value(s) for each model parameter, using the measure of lithospheric flexure that provided the tightest constraints.

To consider the effects of the variance within measurements of lithospheric flexure, we repeated the analyses described above but substituted $\hat{x}_{h,r,m}$ for $(\hat{x}_{h,r,m} - \sigma(\hat{x}_{h,r,m}))$ and then $(\hat{x}_{h,r,m} + \sigma(\hat{x}_{h,r,m}))$, where σ is the standard deviation of the observation (values of σ defined in Section 2.1). The best-fitting parameter values are displayed in Figures S3 - S5 and results of statistical tests are within Table S3. There was good correspondence between the best-fitting parameter values inferred using edifice height (comparison to $\hat{x}_h - \sigma(\hat{x}_h)$, \hat{x}_h and $\hat{x}_h + \sigma(\hat{x}_h)$, residuals \tilde{e}_h), and edifice radius (comparison to $\hat{x}_r - \sigma(\hat{x}_r)$, \hat{x}_r and $\hat{x}_r + \sigma(\hat{x}_r)$, residuals \tilde{e}_r). For these cases, the ranges of best-fitting values of parameters generally intersected. However, when variance in flexural moat width was considered, there were significant differences in the best-fitting values of initial edifice radius, edifice density, lithosphere thickness and lithosphere Young's modulus. Consequently, there were also significant differences in the best-fitting values of these parameters that could be inferred using \tilde{e} .

5.3. Interdependence of model parameters

The best-fitting values of each model parameter were affected by values of other parameters. Figure 8 shows the mean \tilde{e} for each tested value of each parameter (10,000 values averaged for each point, 100 points contoured on each plot). The best-fitting value of initial edifice radius was well constrained at around 383 km, regardless of the values of edifice density, lithosphere thickness, lithosphere Young's modulus and asthenosphere density. Likewise, mean \tilde{e} for tested values of asthenosphere density were unaffected by the values of the other five parameters. However, there was interdependence in the best-fitting values of edifice density, lithosphere thickness and lithosphere Young's modulus. Overall, the best-fitting value of edifice density was between 1833 and 2667 kg.m⁻³ (Figure 6), but as the Young's modulus of the lithosphere increased from 30.6 to 56.1 GPa, the best-fitting value of edifice density increased from 2111 to 2667 kg.m⁻³. Similarly, the overall best-fitting value of lithosphere thickness was between 83.3 and 97.8 km (Figure 6), yet as lithosphere Young's modulus increased from 17.8 to 107.2 GPa, the best-fitting value of lithosphere thickness decreased from 126.7 to 68.9 km.

6. Discussion

The lithosphere deforms under gravitational loading from a volcanic edifice, and this deformation is affected by physical properties of the volcanic edifice, lithosphere and underlying asthenosphere. Finite element models were used to predict the lithospheric flexure at Olympus Mons for a combination of values of model parameters.

6.1. Parameters affecting deformation

Eleven model parameters (asthenosphere density, lithosphere thickness, density, Young's

modulus and Poisson's ratio, edifice initial height, initial radius, density, Young's modulus and Poisson's ratio, and the coefficient of friction between the edifice and lithosphere) were interrogated, and all had an effect on lithospheric flexure (Figure 5). The parameters with the most influence on deformation should be most carefully defined within models of lithospheric flexure, and within deformation models more generally. Most of the model parameters that were interrogated have been considered previously. Values for the edifice volume (dictated by the modeled initial edifice geometry, Section 4.3.1) and lithosphere thickness have been evaluated using analytical modeling (e.g. Isherwood et al., 2013), finite element modeling (e.g. Musiol et al., 2016) and gravitational admittance (e.g. Beuthe et al., 2012). The best-fitting values for densities (of the asthenosphere, lithosphere and edifice) have been constrained using analytical models (e.g. Goettel, 1981), geochemical analyses of Martian meteorites (e.g. Baratoux et al., 2014), gravitational admittance (e.g. Goossens et al., 2017) and shallow radar surveys (Ganesh et al., 2020). Numerical modeling has been used to suggest values for Poisson's ratios of the lithosphere and edifice (Dimitrova and Haines, 2013; Musiol et al., 2016). However, the sensitivity of lithospheric flexure to the Young's modulus of the lithosphere and edifice has not been considered. These parameters ranked 2nd and 7th respectively (maximum 11) for their overall effect on lithospheric flexure; a higher ranking than the Poisson's ratios of the lithosphere and edifice, and the coefficient of friction between the lithosphere and edifice, three parameters that have been previously investigated. Thus, the influence that the Young's modulus has on lithospheric flexure may have previously been underestimated, and assigning accurate values of Young's modulus to model components may warrant greater attention in future.

6.2. Measuring lithospheric flexure

The constraints that could be placed on values of parameters were affected by how lithospheric flexure was quantified - whether edifice height, edifice radius or flexural moat width were evaluated (residuals \tilde{e}_h , \tilde{e}_r and \tilde{e}_m). As expected, the best-fitting values of model parameters were typically most tightly constrained by analysing the residuals from the measure of lithospheric flexure (x_h , x_r , x_m) that they had the greatest effect on. For example, lithosphere thickness had the greatest influence on flexural moat width (Figure 5), and using the residual from flexural moat width, \tilde{e}_m , a unique best-fitting value for lithosphere thickness (83.3 km) was obtained, whereas a range of values were obtained when \tilde{e}_h and \tilde{e}_r were analysed (Figure 7). Overall, values for parameters that define the edifice (initial radius and density) were most tightly constrained from observations of the edifice, whereas values that define lithosphere properties (thickness and Young's modulus) were best constrained using flexural moat width (Young's modulus was equally best constrained using \tilde{e}_h and \tilde{e}_m). Thus, we suggest that the model parameter under investigation should dictate which measure of lithospheric flexure is analysed. This methodology could improve the constraints that previous studies have placed on model properties. For example, Isherwood et al. (2013) used observations of the width of Olympus Mons' flexural moat to infer the density of the edifice and the thickness of the underlying elastic lithosphere. The authors found that a range of values were permissible for both parameters. We suggest that the width of the flexural moat can be used to estimate lithosphere thickness, but cannot place tight constraints on edifice density; comparing the modeled and observed edifice morphology could reduce the range of permissible values for edifice density.

6.3. Constraining model parameters

We found that values for some model parameters could be constrained, under certain conditions. However, not all parameters could be constrained, and the best-fitting values of parameters were dictated by how lithospheric flexure was measured (Section 6.2), whether variance in observations of lithospheric flexure were considered, and the values of other model parameters.

The best-fitting values were defined using the residual that placed the tightest constraint on each model parameter (Table 2), and these results typically correspond with values proposed by previous studies. The combination of the best-fitting value of initial edifice radius (383 km) and the control value of initial edifice height (105 km), results in a peak lithosphere displacement of 10.9 ± 5.6 km (mean \pm standard deviation), which is in agreement with Musiol et al. (2016). Our best-fitting value for lithosphere Young's modulus was 17.8 GPa, which is substantially lower than values used in previous studies (typically 100–120 GPa, e.g. McGovern et al., 2002; Belleguic et al., 2005; Beuthe et al., 2012; Isherwood et al., 2013; Musiol et al., 2016), but corresponds with results from Heap et al. (2017) and Heap et al. (2020). Heap et al. (2020) suggest that 5.4 GPa is an appropriate value of Young's modulus for a volcanic rock with average porosity and fracture density. This is a result for a shallow, terrestrial lithology; Young's modulus increases with depth as rock becomes stiffer, but the average Young's modulus for an identically-sized section of lithosphere on Mars would be less than on Earth, because Mars has a lower surface gravity and consequently a more porous, fractured, weaker lithosphere (Heap et al., 2017). Thus, our value of 17.8 GPa for the Young's modulus of the Martian lithosphere is not unrealistic, and suggests that the widespread upscaling errors for Young's modulus suggested by Heap et al. (2020) could be a phenomenon that extends beyond terrestrial studies.

Our result for lithosphere Young's modulus can also explain the differences between the results of our models and previous studies for values of edifice density and lithosphere thickness. Our best-fitting value for lithosphere thickness (83.3 km) lies within the range of some previous studies (e.g. Belleguic et al., 2005), but is greater than estimates made by McKenzie et al. (2002) and Isherwood et al. (2013). The average value of Young's modulus used in our models (62.5 GPa, Table 1) is lower than the values used in many studies, including McKenzie et al. (2002) (144 GPa) and Isherwood et al. (2013) (100 GPa). We found a negative correlation between lithosphere thickness and lithosphere Young's modulus (Figure 8). Consequently, our best-fitting value of lithosphere thickness is predictably greater than values proposed by previous studies. Similarly, our best fitting values for edifice density (2111–2389 kg.m^{-3}) are within the lower half of the range proposed by Ganesh et al. (2020), but lower than estimates made by McGovern et al. (2002, 2004) and Belleguic et al. (2005). The values of lithosphere Young's modulus within these studies (100 GPa in both cases) are larger than the mean value used in our models, and there is a positive correlation between edifice density and lithosphere Young's modulus (Figure 8), thus it is expected that our best-fitting value for edifice density is less than these studies suggest.

The best-fitting values for initial edifice radius, edifice density, lithosphere thickness and lithosphere Young's modulus were dependent on whether flexure was considered using \tilde{e}_h , \tilde{e}_r or \tilde{e}_m , and were affected by the variance in observed measurements of Olympus Mons' topography (quantified using edifice height, \hat{x}_h , edifice radius, \hat{x}_r , and flexural moat width, \hat{x}_m). Variation between parameter values inferred using \tilde{e}_h , \tilde{e}_r and \tilde{e}_m is attributed to measures of lithospheric flexure being differently affected by different model parameters (Section 6.2). Differences

between the values of parameters inferred using the three measures of lithospheric flexure are attributed to the simplicity of our models. Our model contained a simple, conical edifice. This allowed us to relatively quickly compute the gravity-driven deformation for 100,000 combinations of values of model parameters. However, our inferences about best-fitting values of model parameters assumed that the Olympus Mons edifice, and encircling flexural moat, were radially symmetric. This is an oversimplification. Olympus Mons lies on the flank of the Tharsis rise (McGovern and Morgan, 2009); the northwest of the edifice is at a lower elevation than the southeast and this has affected the morphology of the edifice and the infill of the flexural moat. In addition, the Tharsis rise, which has lateral and vertical dimensions ten times those of Olympus Mons (Figure 1, Borgia and Murray, 2010), has caused downflexure of the lithosphere and is surrounded by a flexural moat (Phillips, 2001). Lithospheric flexure from gravitational loading of Olympus Mons' edifice is therefore superimposed upon much larger-scale lithospheric flexure. These large-scale heterogeneities that underlie the Olympus Mons region become increasingly significant as observations are made over a larger area. Thus, it is unexpected that the values for the measure of lithospheric flexure that cover the greatest spatial extent - flexural moat width - have the greatest variance ($\sigma(\hat{x}_m) = 0.32\hat{x}_m$ whereas $\sigma(\hat{x}_{h,r}) < 0.10\hat{x}_{h,r}$). Consequently, the difference between the best-fitting values of model parameters when \tilde{e}_m was computed using $\hat{x}_m - \sigma(\hat{x}_m)$, \hat{x}_m and $\hat{x}_m + \sigma(\hat{x}_m)$ was greater than when variance within \hat{x}_h and \hat{x}_r was considered. The range of best-fitting parameter values may be reduced with further modeling that incorporates the heterogeneity of the topography underlying Olympus Mons.

6.4. Implications for Mars' subsurface and beyond

The Young's modulus reports the ratio of stress to strain in a material. The Young's modulus of a rock depends on properties of its environment - temperature and pressure - and on its physical attributes - principally its porosity (Heap et al., 2020). We find that the Martian lithosphere, at least in the vicinity of Olympus Mons, has a lower Young's modulus, and thus responds to an applied stress with a greater amount of deformation than has been assumed in previous studies. We consider three wider implications that this has for the Martian lithosphere. First, if the Martian lithosphere is less stiff because it is more porous than has been hitherto proposed, these porous regions could act as subsurface fluid reservoirs. In Mars' early history, these fluid reservoirs may have contained the liquid water that has been preserved within hydrous minerals (e.g. Mustard et al., 2008). Mars is also hypothesized to have experienced large outburst floods, as evidenced from bedrock canyons (e.g. Larsen and Lamb, 2016; Lapotre et al., 2016). Subsurface fluid reservoirs may have provided storage for liquid water, which was rapidly released under pressure and caused these floods (Carr, 1979). Second, if the Martian lithosphere has greater permeability than can be inferred from previous values of Young's modulus, this could increase the volume of fluid transport through the subsurface. Hydrothermal groundwater circulation systems have been proposed as a mechanism for clay formation, and some fossilized conduits have been identified within MOLA elevation data (Ehlmann et al., 2011; Saper and Mustard, 2013). Relatively high subsurface permeability would be required to sustain these systems. This greater permeability could also be exploited by magma, and contribute to the large-scale volcanism that has occurred on Mars (e.g. Heap et al., 2017). Third, there is a trade-off between lithosphere thickness and lithosphere Young's modulus; the same deformation can be produced by a thick lithosphere with a low Young's modulus and a thin lithosphere and a high

Young's modulus. If the Young's modulus is lower than has been thought previously, the thickness of the lithosphere must be greater. This could, in turn, alter the values that are inferred for other parameters that define the Martian subsurface.

Our inferred result for the Young's modulus of the lithosphere aligns with findings by Heap et al. (2020), and suggests that upscaling errors within deformation models are not only constrained to Earth. As for Mars, if the values of Young's modulus assigned to the lithosphere within terrestrial models of lithospheric flexure have been overestimated, the best-fitting values for other parameters including lithosphere thickness and edifice density will be affected. However, terrestrial studies benefit from a range of additional data that cannot be obtained from Mars; Earth's lithosphere surface can be identified within seismic reflection surveys (e.g. Watts et al., 1985), and the material properties of rock samples can be defined quantitatively using laboratory testing (e.g. Manghnani and Woollard, 1965). Consequently, compared to Martian models, terrestrial models of lithospheric flexure, and deformation models more generally, have a reduced number of unconstrained parameters, as well as tighter constraints on values of model parameters. Nevertheless, our results provide additional justification for careful determination of model parameters within all deformation models, and demonstrate the effects that ill-defined model parameters can have on inferences made from deformation models.

7. Conclusions

Finite element models were used to simulate the response of the Martian lithosphere to gravitational loading from the volcanic edifice of Olympus Mons. Model results were first used to establish which of eleven interrogated model parameters (asthenosphere density, lithosphere thickness, density, Young's modulus and Poisson's ratio, edifice initial height, initial radius, density, Young's modulus and Poisson's ratio, and the coefficient of friction between the edifice and lithosphere) had the greatest effect on lithospheric flexure. The five parameters with the greatest effect on flexure (asthenosphere density, lithosphere thickness and Young's modulus and edifice initial radius and density) were then simultaneously varied to constrain their best-fitting values at Olympus Mons. The morphological features used to quantify lithospheric flexure at Olympus Mons affected the best-fitting values of model parameters. Properties of the edifice were most tightly constrained by comparing modeled and observed edifice morphology; using edifice height and radius the best-fitting value for edifice volume (this includes edifice material that now fills the lithosphere depression) were $1.6 \times 10^{16} \text{ m}^3$, and for edifice density the best fitting values were 2111–2389 kg.m^{-3} . Properties of the lithosphere were most tightly constrained by comparing modeled and observed lithosphere morphology; using flexural moat width the best-fitting values for lithosphere thickness and Young's modulus were 83.3 km and 17.8 GPa respectively. Our inferred value of lithosphere Young's modulus is lower than has been hitherto supposed. We propose that the Martian lithosphere is relatively porous and permeable, and that this porosity and permeability could provide a mechanism for fluid storage and transport in Mars' early history. In addition, there is interdependence between the best-fitting values of model parameters, such that reducing the value of Young's modulus has an effect on edifice density and lithosphere thickness; our inferred values for these parameters were at the extremities of typical results of previous studies.

The ability of our methodology to place tight constraints on values for model parameters was limited by the topographic heterogeneity that underlies the Olympus Mons region. Further modeling is required to distinguish this heterogeneity from topography that is directly associated

with flexure beneath Olympus Mons. Additional constraints might be placed on the values of lithosphere dimensions and material properties if the complexity of the model geometry was increased to better represent the Martian surface, and when additional data relating to Mars' subsurface become available, for example from NASA's InSight mission.

Acknowledgments

We thank James Hickey, an anonymous reviewer and the Associate Editor for their helpful comments that improved this manuscript. We thank Jade Eyles and Bridie Davies for support throughout the project. N.T. is supported by the Natural Environment Research Council through the EnvEast Doctoral Training Partnership (NE/L002582/1).

CRedit authorship contribution statement

Nicola Taylor: data curation, formal analysis, investigation, methodology, resources, software, validation, visualization, writing – original draft, writing – review and editing. Jessica Johnson: conceptualization, funding acquisition, investigation, methodology, project administration, resources, software, supervision, writing – review and editing. Richard Herd: funding acquisition, investigation, methodology, resources, supervision, writing – review and editing. Catherine Regan: conceptualization, investigation, methodology, resources, writing – review and editing.

Figure 1: Colorized elevation map showing Olympus Mons lies on the northwest flank of the Tharsis rise. It is encircled by a flexural moat (dashed black line). Inset: locations of topographic profiles (elevations plotted in Figure 3), each profile is 1500 km long. Elevation data collected from MOLA, plotted on a Mercator projection, basemap from NASA (2000).

Figure 2: Deformation of a volcanic edifice under gravity-driven deformation process in profile (left) and map (right) views. (a) Under gravitational sagging, the edifice (green) and lithosphere (grey) are coupled and deform as one unit; inward movement of the edifice causes faulting (including flank terraces) and a flexural moat and bulge surround the edifice. (b) Under gravity-driven volcano spreading, the edifice and lithosphere are decoupled; outward movement of the edifice causes faulting (leaf grabens and a basal scarp). Dashed lines show the shape of the edifice and lithosphere prior to deformation, arrows indicate the direction of movement of edifice and lithosphere and half-arrows relative movement on faults. Ticks are on the downthrown side of faults. Adapted from Byrne et al. (2013).

Figure 3: Topographic profiles for Olympus Mons. Solid lines show elevations with data plotted every 3.69 km, and dashed lines the 39 km-moving average. Data have been adjusted to a reference 0 m elevation at the base of the edifice. Volcanic deposits obscure the flexural moat for west and northwest profiles. The average plot displays the mean values of edifice height, edifice radius and flexural moat width. Six-times vertical exaggeration. MOLA-derived data are plotted, retrieved from Christensen et al. (2009).

Figure 4: Model setup and measured deformation parameters. (a) A solid, elastic edifice overlays the solid, elastic lithosphere and the asthenosphere provides an upwards buoyancy force. There is a frictional interface between the edifice and the lithosphere and a roller boundary is applied to the right boundary. A body load is applied to the edifice. Dashed black line shows axis of symmetry. (b) When gravitational loading is applied to the edifice (instantaneous loading), the edifice and lithosphere deform. We measure the final edifice height, x_h , final edifice radius, x_r , and the width of the flexural moat, x_m , in the model, assuming that the infill of the flexural moat does not reach the elevation of the flexural bulge. Dotted lines show the pre-deformed model geometry. Not to scale.

	Parameter	Control value	Range of values	Tested interval	Units
Asthenosphere					
	Density	3450	3300–3600	33.3	kg.m ⁻³
Lithosphere					
	Thickness	105	40–170	14.4	km
	Density	3000	2500–3500	111.1	kg.m ⁻³
	Poisson's ratio	0.195	0.10–0.49	0.043	-
	Young's modulus	62.5	5–120	12.8	GPa
Edifice					
	Radius	360	150–570	46.7	km
	Height	33	21–45	33	km
	Density	2250	1000–3500	278	kg.m ⁻³
	Poisson's ratio	0.195	0.10–0.49	0.043	-
	Young's modulus	45	5–85	8.9	GPa
Friction					
	Frictional coefficient	0.50	0.10–0.90	0.09	-

Table 1: Range of values for each varied model parameter. Values are based on previous studies at Olympus Mons, elsewhere on Mars and at terrestrial basaltic volcanoes (Section 4). Ten equally-spaced values of each model variable are evaluated.

Figure 5: The model parameters that have the greatest influence on lithospheric flexure depend on how lithospheric flexure is quantified. E, L and A refer to the edifice, lithosphere and asthenosphere respectively. Model parameters are ranked in descending order (11 to 1) of their effect on lithospheric flexure, as measured using (a) post-loading edifice height, (b) post-loading edifice radius and (c) the width of the flexural moat. (d) The three ranks are summed (solid line) to establish the parameters with the most effect on lithospheric flexure.

Figure 6: Best-fitting values of parameters are constrained using overall residuals, \tilde{e} , between observed and modeled lithospheric flexure. Residuals are normalised between 0 (no residual) and 3 (maximum residual). Each boxplots represents 10,000 models and shows the median (thick horizontal line), interquartile range (coloured box) and 1.5 times interquartile range (thin horizontal lines). Purple boxes denote parameter values with the smallest \tilde{e} . Green boxes denote parameter values where \tilde{e} is not significantly different ($p > 0.05$) from the minimum \tilde{e} . All p -values displayed in Table S3.

Figure 7: Best-fitting values of parameters depend on how lithospheric flexure is quantified. Symbology as Figure 6. Residuals in (a) post-loading edifice height, \tilde{e}_h , (b) post-loading edifice radius, \tilde{e}_r , and (c) flexural moat width \tilde{e}_m have been normalised between 0 (no residual) and 1 (maximum difference between model and observations). All p -values displayed in Table S3.

Parameter	Model result		Previous studies		
	Residual	Value(s)	Value(s)	Location	Reference
Initial edifice radius (km)					
	\tilde{e}_r	383			
Edifice density (kg.m^{-3})					
	\tilde{e}_h	2111–2389	3150	Olympus Mons	McGovern et al. (2002, 2004)
			3250 ± 150	Olympus Mons	Belleguic et al. (2005)
			1800–3120	Arsia Mons	Ganesh et al. (2020)
Lithosphere thickness (km)					
	\tilde{e}_m	83.3	> 150	Olympus Mons	Comer et al. (1985)
			≈ 70	Tharsis	McKenzie et al. (2002)
			> 70	Olympus Mons	McGovern et al. (2002, 2004)
			93 ± 40	Olympus Mons	Belleguic et al. (2005)
			70–80	Olympus Mons	Isherwood et al. (2013)
Lithosphere Young's modulus (GPa)					
	\tilde{e}_r or \tilde{e}_m	17.8	> 5.4	Terrestrial	Heap et al. (2020)
			144*	Olympus Mons	McKenzie et al. (2002)
			100*	Olympus Mons	Isherwood et al. (2013)

Table 2: Best-fitting values for four model parameters and comparisons to published data. Asterisks (*) indicate values that have been used within, but not derived by, previous studies. Due to our instantaneous model-loading scenario, the best-fitting initial edifice radius cannot be directly compared to previous studies. The best-fitting values for each parameter are determined using the residual (\tilde{e}_h , \tilde{e}_r , \tilde{e}_m are from comparisons of modeled and observed edifice height, edifice radius, flexural moat width respectively) that provided the tightest constraints. A range is provided where there were multiple non-different best-fitting values ($p > 0.05$, all p -values displayed in Table S3).

Figure 8: Interdependence between best-fitting values for some model parameters. Pale and dark colours indicate combinations of model parameters with smaller and larger residuals respectively; a unique colour scale is used for each plot (Figure S6 displays these results with one color scale). Ten values of each parameter are tested (100 points contoured within each plot) and the overall residual is the sum of residuals from edifice height and radius and the width of the flexural moat. The mean residual ($n = 10,000$) is plotted for each tested parameter value.

References

Baratoux, D., Samuel, H., Michaut, C., Toplis, M. J., Monnereau, M., Wiczorek, M., Garcia, R., Kurita, K., 2014. Petrological constraints on the density of the Martian crust. *Journal of Geophysical Research: Planets* 119 (7), 1707–1727.

URL <http://doi.wiley.com/10.1002/2014JE004642>, doi:10.1002/2014JE004642.

Belleguic, V., Lognonné, P., Wiczorek, M., 2005. Constraints on the Martian lithosphere from gravity and topography data. *Journal of Geophysical Research* 110 (E11), E11005.

URL <http://doi.wiley.com/10.1029/2005JE002437>, doi:10.1029/2005JE002437.

Bertka, C. M., Fei, Y., 1997. Mineralogy of the Martian interior up to core-mantle boundary pressures. *Journal of Geophysical Research: Solid Earth* 102 (B3), 5251–5264.

URL <http://doi.wiley.com/10.1029/96JB03270>, doi:10.1029/96JB03270.

Bertka, C. M., Fei, Y., 1998. Density profile of an SNC model Martian interior and the moment-of-inertia factor of Mars. *Earth and Planetary Science Letters* 157 (1-2), 79–88.

URL <https://linkinghub.elsevier.com/retrieve/pii/S0012821X98000302>, doi:10.1016/S0012-821X(98)00030-2.

Beuthe, M., Le Maistre, S., Rosenblatt, P., Pätzold, M., Dehant, V., 2012. Density and lithospheric thickness of the Tharsis Province from MEX MaRS and MRO gravity data. *Journal of Geophysical Research: Planets* 117 (E4), n/a–n/a.

URL <http://doi.wiley.com/10.1029/2011JE003976>, doi:10.1029/2011JE003976.

Borgia, A., Delaney, P. T., Denlinger, R. P., 2000. Spreading Volcanoes. *Annual Review of Earth and Planetary Sciences* 28 (1), 539–570.

URL <http://www.annualreviews.org/doi/10.1146/annurev.earth.28.1.539>, doi:10.1146/annurev.earth.28.1.539.

Borgia, A., Murray, J. B., 2010. Is Tharsis Rise, Mars, a spreading volcano? In: *What Is a Volcano?* Geological Society of America.

URL <https://pubs.geoscienceworld.org/books/book/624/chapter/3805610>, doi:10.101130/2010.2470(08)

Breuer, D., Spohn, T., 2006. Viscosity of the Martian mantle and its initial temperature: Constraints from crust formation history and the evolution of the magnetic field. *Planetary and Space Science* 54 (2), 153–169.

URL <https://linkinghub.elsevier.com/retrieve/pii/S0032063305002163>, doi:10.1016/j.pss.2005.08.008.

Brotchie, J. F., Silvester, R., 1969. On crustal flexure. *Journal of Geophysical Research* 74 (22), 5240–5252.

URL <http://doi.wiley.com/10.1029/JB074i022p05240>, doi:10.1029/JB074i022p05240.

Byrne, P., Holohan, E., Kervyn, M., van Wyk de Vries, B., Troll, V., Murray, J., 2013. A

sagging-spreading continuum of large volcano structure. *Geology* 41 (3), 339–342.

URL <http://pubs.geoscienceworld.org/geology/article/41/3/339/131156/A-sagging-spreading-continuum-of-large-volcano>, doi:10.1130/G33990.1.

Carr, M. H., 1979. Formation of Martian flood features by release of water from confined aquifers. *Journal of Geophysical Research* 84 (B6), 2995.

URL <http://doi.wiley.com/10.1029/JB084iB06p02995>, doi:10.1029/JB084iB06p02995.

Chadwick, J., McGovern, P., Simpson, M., Reeves, A., 2015. Late Amazonian subsidence and magmatism of Olympus Mons, Mars. *Journal of Geophysical Research: Planets* 120 (9), 1585–1595.

URL <http://doi.wiley.com/10.1002/2015JE004875>, doi:10.1002/2015JE004875.

Christensen, P., Engle, E., Anwar, S., Dickenshield, S., Noss, D., Gorelick, N., Weiss-Malik, M., 2009. JMARS - A Planetary GIS.

URL <http://adsabs.harvard.edu/abs/2009AGUFMIN22A..06C>

Collier, J. S., Singh, S. C., 1998. Poisson's ratio structure of young oceanic crust. *Journal of Geophysical Research: Solid Earth* 103 (B9), 20981–20996.

URL <http://doi.wiley.com/10.1029/98JB01980>, doi:10.1029/98JB01980.

Comer, R. P., Solomon, S. C., Head, J. W., 1985. Mars: Thickness of the lithosphere from the tectonic response to volcanic loads. *Reviews of Geophysics* 23 (1), 61–92.

URL <http://doi.wiley.com/10.1029/RG023i001p00061>, doi:10.1029/RG023i001p00061.

Crown, D. A., Ramsey, M. S., 2017. Morphologic and thermophysical characteristics of lava flows southwest of Arsia Mons, Mars. *Journal of Volcanology and Geothermal Research* 342, 13–28.

URL <https://linkinghub.elsevier.com/retrieve/pii/S0377027316302190>, doi:10.1016/j.jvolgeores.2016.07.008.

Del Negro, C., Currenti, G., Scandura, D., 2009. Temperature-dependent viscoelastic modeling of ground deformation: Application to Etna volcano during the 1993–1997 inflation period. *Physics of the Earth and Planetary Interiors* 172 (3-4), 299–309.

URL <https://linkinghub.elsevier.com/retrieve/pii/S0031920108003087>, doi:10.1016/j.pepi.2008.10.019.

Denlinger, R. P., Morgan, J. K., 2014. Instability of Hawaiian Volcanoes. In: *Characteristics of Hawaiian Volcanoes*. U.S. Geological Survey.

Dimitrova, L., Haines, A., 2013. Constraining the Long Term Poisson's Ratio of the Martian Lithosphere From 2D and 3D Dynamic Modeling of Lithospheric Stress and the Surface Faulting Record.

Dorman, L. M., Lewis, B. T. R., 1970. Experimental isostasy: 1. Theory of the determination of the Earth's isostatic response to a concentrated load. *Journal of Geophysical*

Research 75 (17), 3357–3365.

URL <http://doi.wiley.com/10.1029/JB075i017p03357>, doi:10.1029/JB075i017p03357.

Dreibus, G., Wanke, H., 1985. Mars, a volatile-rich planet. *Meteoritics* 20 (2), 367–381.

Ehlmann, B. L., Mustard, J. F., Murchie, S. L., Bibring, J.-P., Meunier, A., Fraeman, A. A., Langevin, Y., 2011. Subsurface water and clay mineral formation during the early history of Mars. *Nature* 479 (7371), 53–60.

URL <http://www.nature.com/articles/nature10582>, doi:10.1038/nature10582.

Folkner, W. M., Yoder, C. F., Yuan, D. N., Standish, E. M., Preston, R. A., 1997. Interior Structure and Seasonal Mass Redistribution of Mars from Radio Tracking of Mars Pathfinder. *Science* 278 (5344), 1749–1752.

URL <http://www.sciencemag.org/lookup/doi/10.1126/science.278.5344.1749>, doi:10.1126/science.278.5344.1749.

Frey, H. V., Roark, J. H., Shockey, K. M., Frey, E. L., Sakimoto, S. E. H., 2002. Ancient lowlands on Mars. *Geophysical Research Letters* 29 (10), 22–1–22–4.

URL <http://doi.wiley.com/10.1029/2001GL013832>, doi:10.1029/2001GL013832.

Ganesh, I., Carter, L. M., Smith, I. B., 2020. SHARAD mapping of Arsia Mons caldera. *Journal of Volcanology and Geothermal Research* 390, 106748.

URL <https://linkinghub.elsevier.com/retrieve/pii/S0377027319303580>, doi:10.1016/j.jvolgeores.2019.106748.

Gercek, H., 2007. Poisson's ratio values for rocks. *International Journal of Rock Mechanics and Mining Sciences* 44 (1), 1–13.

URL <https://linkinghub.elsevier.com/retrieve/pii/S136516090600075X>, doi:10.1016/j.ijrmms.2006.04.011.

Goettel, K. A., 1981. Density of the mantle of Mars. *Geophysical Research Letters* 8 (5), 497–500.

URL <http://doi.wiley.com/10.1029/GL008i005p00497>, doi:10.1029/GL008i005p00497.

Goossens, S., Sabaka, T. J., Genova, A., Mazarico, E., Nicholas, J. B., Neumann, G. A., 2017. Evidence for a low bulk crustal density for Mars from gravity and topography. *Geophysical Research Letters* 44 (15), 7686–7694.

URL <http://doi.wiley.com/10.1002/2017GL074172>, doi:10.1002/2017GL074172.

Grigg, R. W., Jones, A. T., 1997. Uplift caused by lithospheric flexure in the Hawaiian Archipelago as revealed by elevated coral deposits. *Marine Geology* 141 (1-4), 11–25.

URL <https://linkinghub.elsevier.com/retrieve/pii/S0025322797000698>, doi:10.1016/S0025-3227(97)00069-8.

Grott, M., Hauber, E., Werner, S. C., Kronberg, P., Neukum, G., 2005. High heat flux on ancient Mars: Evidence from rift flank uplift at Coracis Fossae. *Geophysical Research Letters* 32

(21), L21201.

URL <http://doi.wiley.com/10.1029/2005GL023894>, doi:10.1029/2005GL023894.

Hauck, S. A., 2002. Thermal and crustal evolution of Mars. *Journal of Geophysical Research* 107 (E7), 5052.

URL <http://doi.wiley.com/10.1029/2001JE001801>, doi:10.1029/2001JE001801.

Heap, M. J., Byrne, P. K., Mikhail, S., 2017. Low surface gravitational acceleration of Mars results in a thick and weak lithosphere: Implications for topography, volcanism, and hydrology. *Icarus* 281, 103–114.

URL <https://linkinghub.elsevier.com/retrieve/pii/S0019103516301609>, doi:10.1016/j.icarus.2016.09.003.

Heap, M. J., Villeneuve, M., Albino, F., Farquharson, J. I., Brothelande, E., Amelung, F., Got, J.-L., Baud, P., 2020. Towards more realistic values of elastic moduli for volcano modelling. *Journal of Volcanology and Geothermal Research* 390, 106684.

URL <https://linkinghub.elsevier.com/retrieve/pii/S0377027319304044>, doi:10.1016/j.jvolgeores.2019.106684.

Houghton, B. F., Wilson, C. J. N., 1989. A vesicularity index for pyroclastic deposits. *Bulletin of Volcanology* 51 (6), 451–462.

URL <http://link.springer.com/10.1007/BF01078811>, doi:10.1007/BF01078811.

Hynek, B. M., Robbins, S. J., Šrámek, O., Zhong, S. J., 2011. Geological evidence for a migrating Tharsis plume on early Mars. *Earth and Planetary Science Letters* 310 (3-4), 327–333.

URL <https://linkinghub.elsevier.com/retrieve/pii/S0012821X11004845>, doi:10.1016/j.epsl.2011.08.020.

Isherwood, R. J., Jozwiak, L. M., Jansen, J. C., Andrews-Hanna, J. C., 2013. The volcanic history of Olympus Mons from paleo-topography and flexural modeling. *Earth and Planetary Science Letters* 363, 88–96.

URL <https://linkinghub.elsevier.com/retrieve/pii/S0012821X12007066>, doi:10.1016/j.epsl.2012.12.020.

Johnston, D. H., McGetchin, T. R., Toksöz, M. N., 1974. The thermal state and internal structure of Mars. *Journal of Geophysical Research* 79 (26), 3959–3971.

URL <http://doi.wiley.com/10.1029/JB079i026p03959>, doi:10.1029/JB079i026p03959.

Johnston, D. H., Toksöz, M., 1977. Internal structure and properties of Mars. *Icarus* 32 (1), 73–84.

URL <https://linkinghub.elsevier.com/retrieve/pii/0019103577900501>, doi:10.1016/0019-1035(77)90050-1.

Kiefer, W. S., 2003. Melting in the martian mantle: Shergottite formation and implications for present-day mantle convection on Mars. *Meteoritics & Planetary Science* 38 (12), 1815–1832.

URL <http://doi.wiley.com/10.1111/j.1945-5100.2003.tb00017.x>,

doi:10.1111/j.1945-5100.2003.tb00017.x.

Kiefer, W. S., Li, Q., 2016. Water undersaturated mantle plume volcanism on present-day Mars. *Meteoritics & Planetary Science* 51 (11), 1993–2010.

URL <http://doi.wiley.com/10.1111/maps.12720>, doi:10.1111/maps.12720.

Kwon, Y.-D., Kwon, S.-B., Lu, X., Kwon, H.-W., 2014. A Finite Element Procedure with Poisson Iteration Method Adopting Pattern Approach Technique for Near-Incompressible Rubber Problems. *Advances in Mechanical Engineering* 6, 272574.

URL <http://journals.sagepub.com/doi/10.1155/2014/272574>, doi:10.1155/2014/272574.

Lapotre, M. G. A., Lamb, M. P., Williams, R. M. E., 2016. Canyon formation constraints on the discharge of catastrophic outburst floods of Earth and Mars: DISCHARGES OF CANYON-CARVING FLOODS OF EARTH AND MARS. *Journal of Geophysical Research: Planets* 121 (7), 1232–1263.

URL <http://doi.wiley.com/10.1002/2016JE005061>, doi:10.1002/2016JE005061.

Larsen, I. J., Lamb, M. P., 2016. Progressive incision of the Channeled Scablands by outburst floods. *Nature* 538 (7624), 229–232.

URL <http://www.nature.com/articles/nature19817>, doi:10.1038/nature19817.

Leone, G., 2016. Alignments of volcanic features in the southern hemisphere of Mars produced by migrating mantle plumes. *Journal of Volcanology and Geothermal Research* 309, 78–95. URL <https://linkinghub.elsevier.com/retrieve/pii/S0377027315003662>, doi:10.1016/j.jvolgeores.2015.10.028.

Leone, G., 2017. Mangala Valles, Mars: A reassessment of formation processes based on a new geomorphological and stratigraphic analysis of the geological units. *Journal of Volcanology and Geothermal Research* 337, 62–80.

URL <https://linkinghub.elsevier.com/retrieve/pii/S0377027316303900>, doi:10.1016/j.jvolgeores.2017.03.011.

Leone, G., Tackley, P. J., Gerya, T. V., May, D. A., Zhu, G., 2014. Three-dimensional simulations of the southern polar giant impact hypothesis for the origin of the Martian dichotomy: Southern Impact for Martian Dichotomy. *Geophysical Research Letters* 41 (24), 8736–8743.

URL <http://doi.wiley.com/10.1002/2014GL062261>, doi:10.1002/2014GL062261.

Manghnani, M. H., Woollard, G. P., 1965. Ultrasonic Velocities and Related Elastic Properties of Hawaiian Basaltic Rocks. *Pacific Science* 19, 291–295.

McGovern, P. J., Grosfils, E. B., Galgana, G. A., Morgan, J. K., Rumpf, M. E., Smith, J. R., Zimbelman, J. R., 2015. Lithospheric flexure and volcano basal boundary conditions: keys to the structural evolution of large volcanic edifices on the terrestrial planets. *Geological Society, London, Special Publications* 401 (1), 219–237.

URL <http://sp.lyellcollection.org/lookup/doi/10.1144/SP401.7>, doi:10.1144/SP401.7.

McGovern, P. J., Morgan, J. K., 2009. Volcanic spreading and lateral variations in the structure of Olympus Mons, Mars. *Geology* 37 (2), 139–142.

URL <http://pubs.geoscienceworld.org/geology/article/37/2/139/519448/Volcanic-spreading-and-lateral-variations-in-the>, doi:10.1130/G25180A.1.

McGovern, P. J., Solomon, S. C., 1993. State of stress, faulting, and eruption characteristics of large volcanoes on Mars. *Journal of Geophysical Research* 98 (E12), 23553.

URL <http://doi.wiley.com/10.1029/93JE03093>, doi:10.1029/93JE03093.

McGovern, P. J., Solomon, S. C., Smith, D. E., Zuber, M. T., Simons, M., Wieczorek, M., Phillips, R. J., Neumann, G. A., Aharonson, O., Head, J. W., 2004. Correction to “Localized gravity/topography admittance and correlation spectra on Mars: Implications for regional and global evolution”. *Journal of Geophysical Research* 109 (E7), E07007.

URL <http://doi.wiley.com/10.1029/2004JE002286>, doi:10.1029/2004JE002286.

McGovern, P. J., Solomon, S. C., Smith, D. E., Zuber, M. T., Simons, M., Wieczorek, M. A., Phillips, R. J., Neumann, G. A., Aharonson, O., Head, J. W., 2002. Localized gravity/topography admittance and correlation spectra on Mars: Implications for regional and global evolution. *Journal of Geophysical Research: Planets* 107 (E12), 19–1–19–25.

URL <http://doi.wiley.com/10.1029/2002JE001854>, doi:10.1029/2002JE001854.

McKenzie, D., Barnett, D. N., Yuan, D.-N., 2002. The relationship between Martian gravity and topography. *Earth and Planetary Science Letters* 195 (1-2), 1–16.

URL <https://linkinghub.elsevier.com/retrieve/pii/S0012821X01005556>, doi:10.1016/S0012-821X(01)00555-6.

McSween, H. Y., Taylor, G. J., Wyatt, M. B., 2009. Elemental Composition of the Martian Crust. *Science* 324 (5928), 736–739.

URL <http://www.sciencemag.org/cgi/doi/10.1126/science.1165871>, doi:10.1126/science.1165871.

Moore, J. G., 2001. Density of basalt core from Hilo drill hole, Hawaii. *Journal of Volcanology and Geothermal Research* 112 (1-4), 221–230.

URL <https://linkinghub.elsevier.com/retrieve/pii/S0377027301002426>, doi:10.1016/S0377-0273(01)00242-6.

Musiol, S., Holohan, E. P., Cailleau, B., Platz, T., Dumke, A., Walter, T. R., Williams, D. A., van Gasselt, S., 2016. Lithospheric flexure and gravity spreading of Olympus Mons volcano, Mars. *Journal of Geophysical Research: Planets* 121 (3), 255–272.

URL <http://doi.wiley.com/10.1002/2015JE004896>, doi:10.1002/2015JE004896.

Mustard, J. F., Murchie, S. L., Pelkey, S. M., Ehlmann, B. L., Milliken, R. E., Grant, J. A., Bibring, J.-P., Poulet, F., Bishop, J., Dobra, E. N., Roach, L., Seelos, F., Arvidson, R. E., Wiseman, S., Green, R., Hash, C., Humm, D., Malaret, E., McGovern, J. A., Seelos, K., Clancy, T., Clark, R., Marais, D. D., Izenberg, N., Knudson, A., Langevin, Y., Martin, T., McGuire, P., Morris, R., Robinson, M., Roush, T., Smith, M., Swayze, G., Taylor, H., Titus, T., Wolff, M.,

2008. Hydrated silicate minerals on Mars observed by the Mars Reconnaissance Orbiter CRISM instrument. *Nature* 454 (7202), 305–309.

URL <http://www.nature.com/articles/nature07097>, doi:10.1038/nature07097.

NASA, 2000. The Topography of Mars by the Mars Orbiter Laser Altimeter (MOLA).

URL <https://attic.gsfc.nasa.gov/mola/images.html>

Neukum, G., Hoffmann, H., Hauber, E., Head, J. W., Basilevsky, A. T., Ivanov, B. A., Werner, S. C., van Gasselt, S., Murray, J. B., McCord, T., 2004. Recent and episodic volcanic and glacial activity on Mars revealed by the High Resolution Stereo Camera. *Nature* 432 (7020), 971–979. URL <http://www.nature.com/articles/nature03231>, doi:10.1038/nature03231.

Neumann, G. A., 2004. Crustal structure of Mars from gravity and topography. *Journal of Geophysical Research* 109 (E8), E08002.

URL <http://doi.wiley.com/10.1029/2004JE002262>, doi:10.1029/2004JE002262.

Okal, E. A., Anderson, D. L., 1978. Theoretical models for Mars and their seismic properties. *Icarus* 33 (3), 514–528. URL <https://linkinghub.elsevier.com/retrieve/pii/0019103578901872>, doi:10.1016/0019-1035(78)90187-2.

O'Rourke, J. G., Korenaga, J., 2012. Terrestrial planet evolution in the stagnant-lid regime: Size effects and the formation of self-destabilizing crust. *Icarus* 221 (2), 1043–1060.

URL <https://linkinghub.elsevier.com/retrieve/pii/S0019103512004228>, doi:10.1016/j.icarus.2012.10.015.

Pauer, M., Breuer, D., 2008. Constraints on the maximum crustal density from gravity–topography modeling: Applications to the southern highlands of Mars. *Earth and Planetary Science Letters* 276 (3-4), 253–261.

URL <https://linkinghub.elsevier.com/retrieve/pii/S0012821X08005992>, doi:10.1016/j.epsl.2008.09.014.

Phillips, R. J., 2001. Ancient Geodynamics and Global-Scale Hydrology on Mars. *Science* 291 (5513), 2587–2591.

URL <http://www.sciencemag.org/cgi/doi/10.1126/science.1058701>, doi:10.1126/science.1058701.

Plescia, J. B., 2004. Morphometric properties of Martian volcanoes. *Journal of Geophysical Research* 109 (E3), E03003.

URL <http://doi.wiley.com/10.1029/2002JE002031>, doi:10.1029/2002JE002031.

Robbins, S. J., Achille, G. D., Hynes, B. M., 2011. The volcanic history of Mars: High-resolution crater-based studies of the calderas of 20 volcanoes. *Icarus* 211 (2), 1179–1203.

URL <https://linkinghub.elsevier.com/retrieve/pii/S00191035110004318>, doi:10.1016/j.icarus.2010.11.012.

Saper, L., Mustard, J. F., 2013. Extensive linear ridge networks in Nili Fossae and

Nilosyrtris, Mars: implications for fluid flow in the ancient crust: INVERTED LINEAR RIDGE NETWORKS ON MARS. *Geophysical Research Letters* 40 (2), 245–249.

URL <http://doi.wiley.com/10.1002/grl.50106>, doi:10.1002/grl.50106.

Schumacher, S., Breuer, D., 2007. An alternative mechanism for recent volcanism on Mars. *Geophysical Research Letters* 34 (14), L14202.

URL <http://doi.wiley.com/10.1029/2007GL030083>

[Smith(1999)] Smith, D. E., 1999. The Global Topography of Mars and Implications for Surface Evolution. *Science* 284 (5419), 1495–1503.

URL <http://www.sciencemag.org/cgi/doi/10.1126/science.284.5419.1495>, doi:10.1126/science.284.5419.1495.

Smith, D. E., Zuber, M. T., Frey, H. V., Garvin, J. B., Head, J. W., Muhleman, D. O., Pettengill, G. H., Phillips, R. J., Solomon, S. C., Zwally, H. J., Banerdt, W. B., Duxbury, T. C., Golombek, M. P., Lemoine, F. G., Neumann, G. A., Rowlands, D. D., Aharonson, O., Ford, P. G., Ivanov, A. B., Johnson, C. L., McGovern, P. J., Abshire, J. B., Afzal, R. S., Sun, X., 2001. Mars Orbiter Laser Altimeter: Experiment summary after the first year of global mapping of Mars. *Journal of Geophysical Research: Planets* 106 (E10), 23689–23722.

URL <http://doi.wiley.com/10.1029/2000JE001364>, doi:10.1029/2000JE001364.

Tesauro, M., Audet, P., Kaban, M. K., Bürgmann, R., Cloetingh, S., 2012. The effective elastic thickness of the continental lithosphere: Comparison between rheological and inverse approaches. *Geochemistry, Geophysics, Geosystems* 13 (9).

URL <http://doi.wiley.com/10.1029/2012GC004162>, doi:10.1029/2012GC004162.

Watts, A. B., 2001. *Isostasy and Flexure of the Lithosphere*. Cambridge University Press.

Watts, A. B., ten Brink, U. S., Buhl, P., Brocher, T. M., 1985. A multichannel seismic study of lithospheric flexure across the Hawaiian–Emperor seamount chain. *Nature* 315 (6015), 105–111. URL <http://www.nature.com/articles/315105a0>, doi:10.1038/315105a0.

Weller, M. B., McGovern, P. J., Fournier, T., Morgan, J. K., 2014. Eastern Olympus Mons Basal Scarp: Structural and mechanical evidence for large-scale slope instability: OLYMPUS MONS BASAL SCARP INSTABILITY. *Journal of Geophysical Research: Planets* 119 (6), 1089–1109. URL <http://doi.wiley.com/10.1002/2013JE004524>, doi:10.1002/2013JE004524.

Wenzel, M. J., 2004. Tharsis as a consequence of Mars' dichotomy and layered mantle. *Geophysical Research Letters* 31 (4), L04702. URL <http://doi.wiley.com/10.1029/2003GL019306>, doi:10.1029/2003GL019306.

Williams, J.-P., Nimmo, F., Moore, W. B., Paige, D. A., 2008. The formation of Tharsis on Mars: What the line-of-sight gravity is telling us. *Journal of Geophysical Research* 113 (E10), E10011. URL <http://doi.wiley.com/10.1029/2007JE003050>, doi:10.1029/2007JE003050.

Wilson, L., Scott, E. D., Head, J. W., 2001. Evidence for episodicity in the magma supply to the large Tharsis volcanoes. *Journal of Geophysical Research: Planets* 106 (E1), 1423–1433. URL <http://doi.wiley.com/10.1029/2000JE001280>, doi:10.1029/2000JE001280.

Yoder, C. F., Standish, E. M., 1997. Martian precession and rotation from Viking lander range data. *Journal of Geophysical Research: Planets* 102 (E2), 4065–4080. URL <http://doi.wiley.com/10.1029/96JE03642>, doi:10.1029/96JE03642.

Zhong, S., 2009. Migration of Tharsis volcanism on Mars caused by differential rotation of the lithosphere. *Nature Geoscience* 2 (1), 19–23. URL <http://www.nature.com/articles/ngeo392>, doi:10.1038/ngeo392.

Zhong, S., Watts, A. B., 2013. Lithospheric deformation induced by loading of the Hawaiian Islands and its implications for mantle rheology. *Journal of Geophysical Research: Solid Earth* 118 (11), 6025–6048. URL <http://doi.wiley.com/10.1002/2013JB010408>, doi:10.1002/2013JB010408.

AuthorStatement

Nicola Taylor: data curation, formal analysis, investigation, methodology, resources, software, validation, visualization, writing – original draft, writing – review and editing.

Jessica Johnson: conceptualization, funding acquisition, investigation, methodology, project administration, resources, software, supervision, writing – review and editing.

Richard Herd: funding acquisition, investigation, methodology, resources, supervision, writing – review and editing.

Catherine Regan: conceptualization, investigation, methodology, resources, writing – review and editing.

Journal Pre-proof

Declaration of interests

The authors declare that they have no known competing financial interests or personal relationships that could have appeared to influence the work reported in this paper.

The authors declare the following financial interests/personal relationships which may be considered as potential competing interests:

Journal Pre-proof

Highlights

We use FEA to constrain physical properties of Olympus Mons and Mars' lithosphere

We constrain the Young's modulus of the Martian lithosphere for the first time

Mars' lithosphere is less stiff and may be more porous than was previously assumed

Journal Pre-proof

Elevation (km)

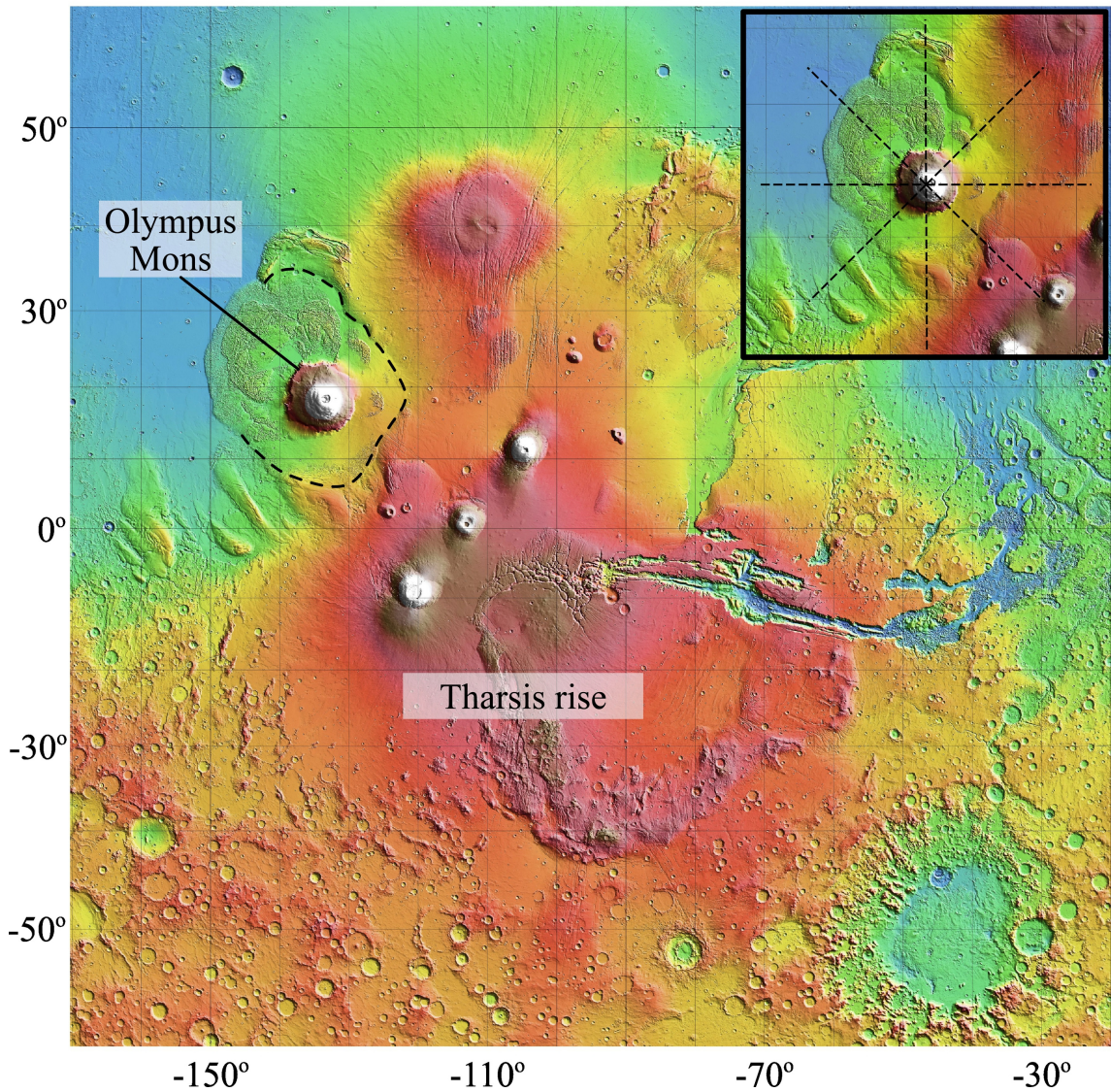
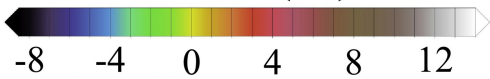


Figure 1

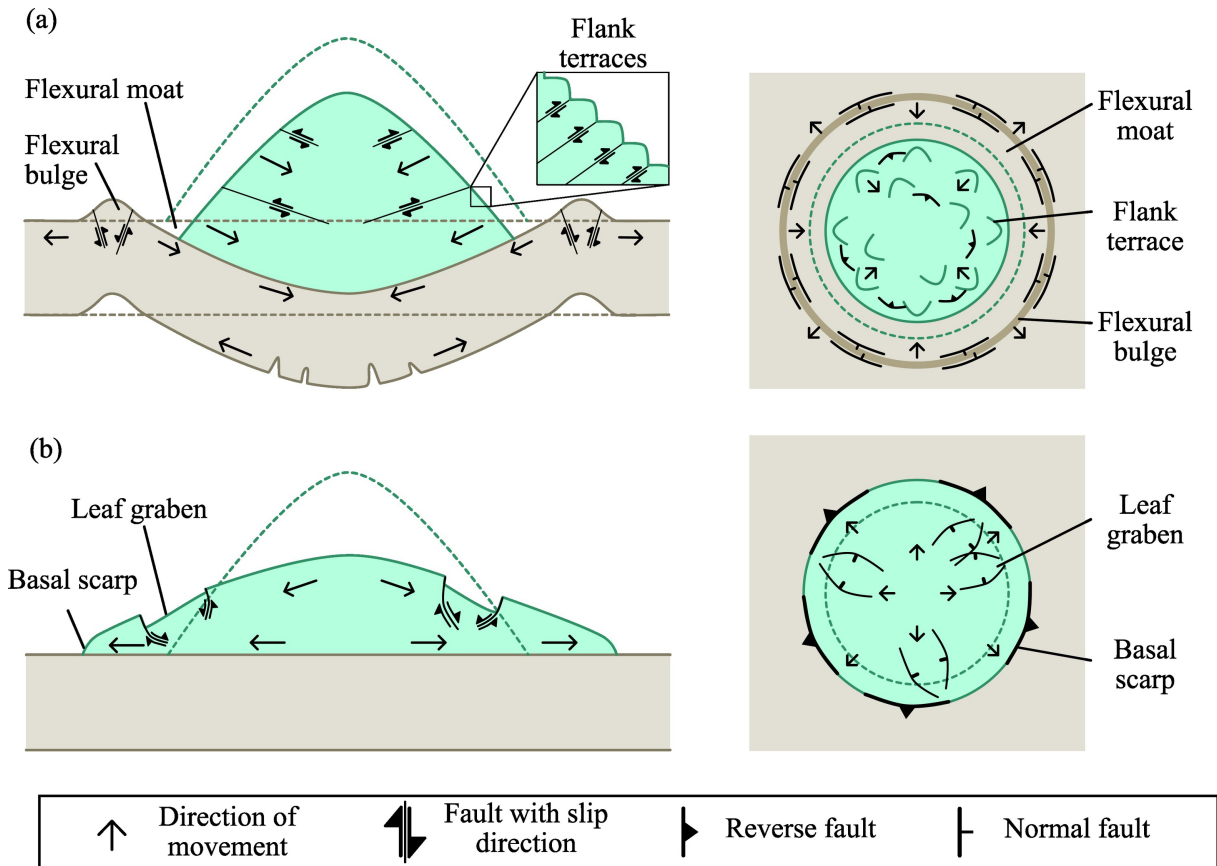


Figure 2

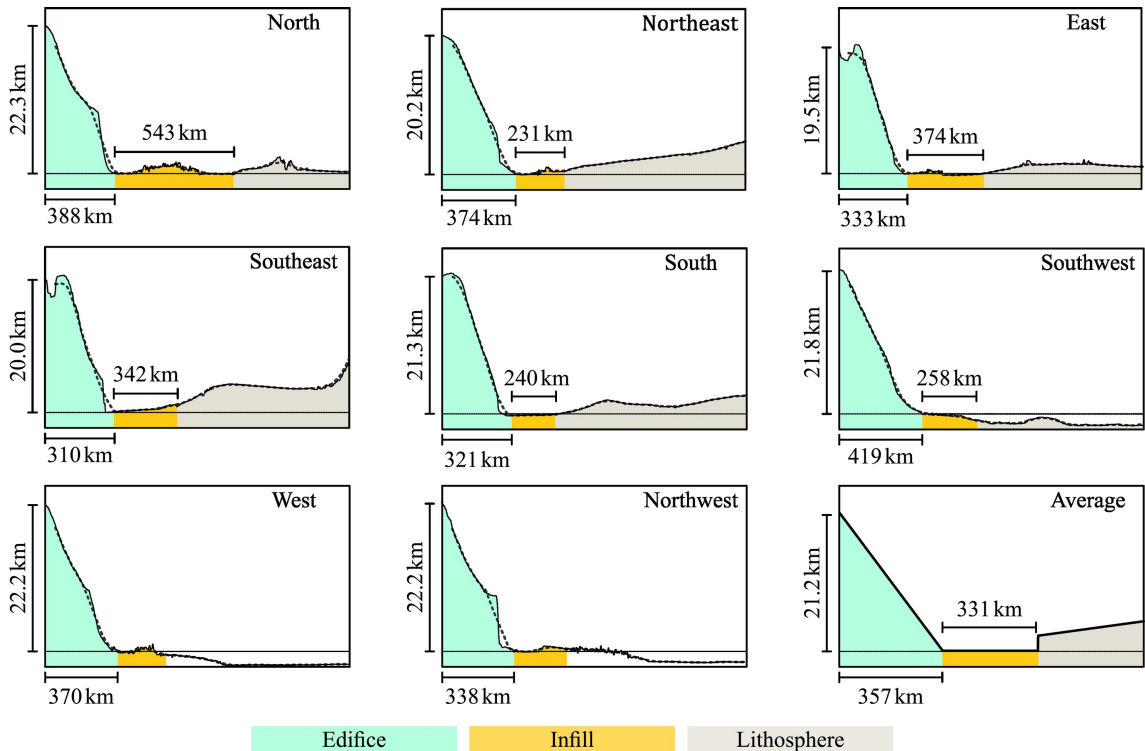


Figure 3

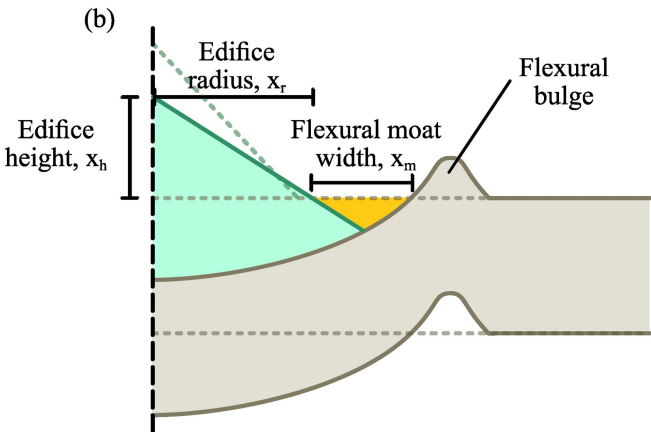
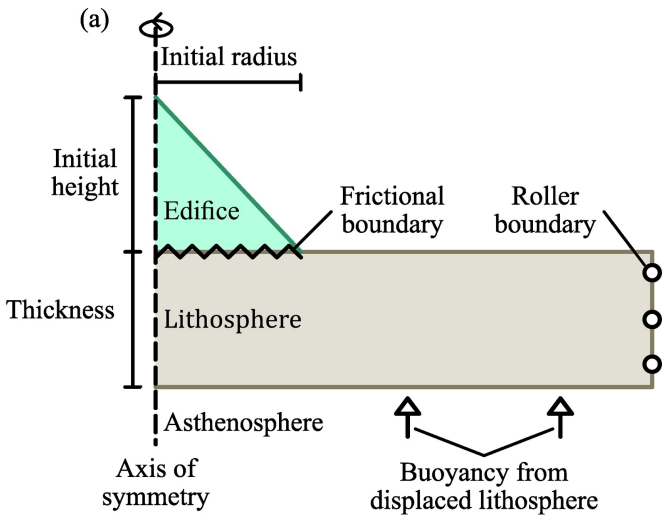


Figure 4

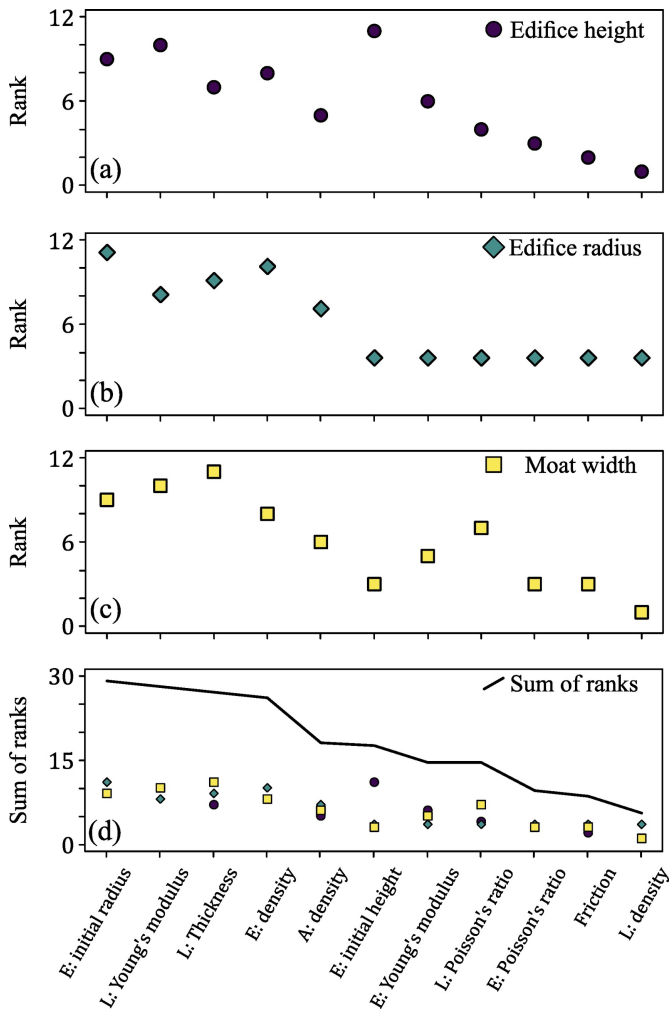


Figure 5

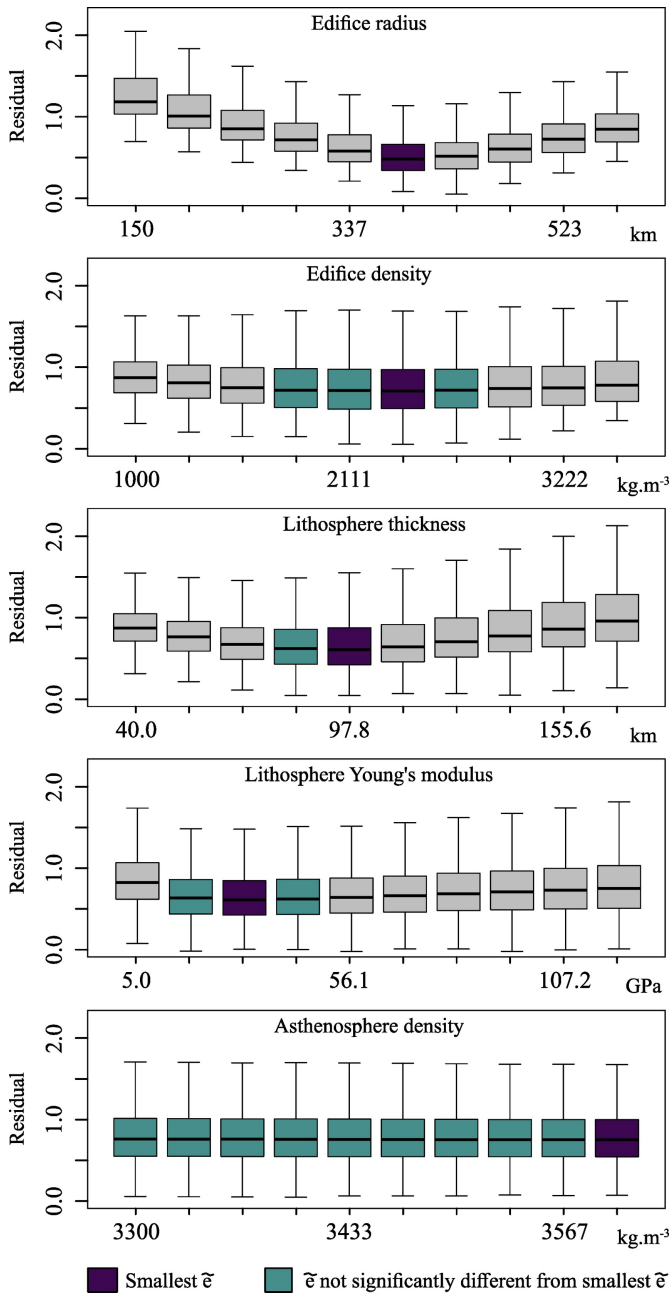


Figure 6

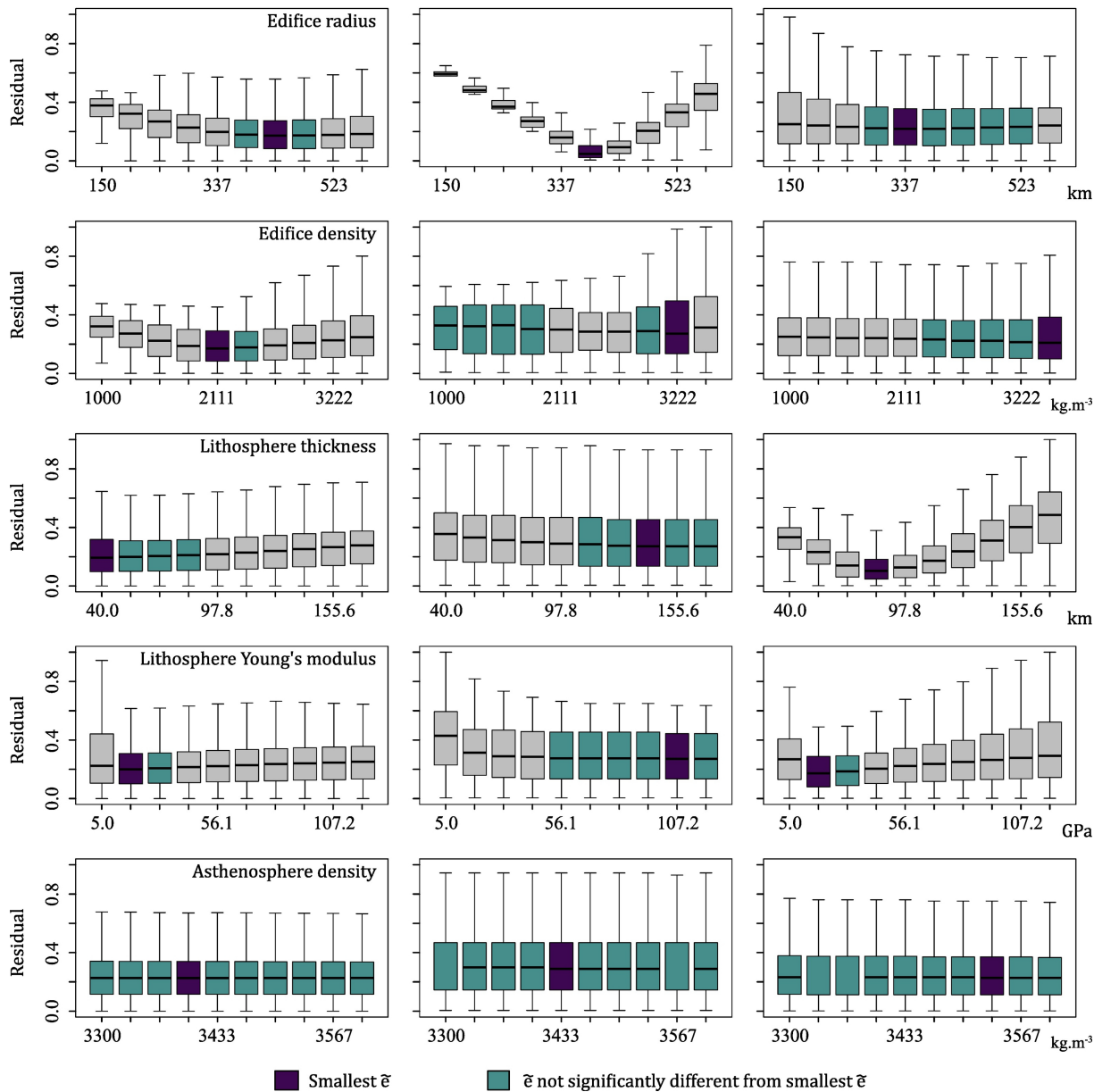
(a) Residual: $\tilde{\epsilon}_n$ (b) Residual: $\tilde{\epsilon}_t$ (c) Residual: $\tilde{\epsilon}_m$ 

Figure 7

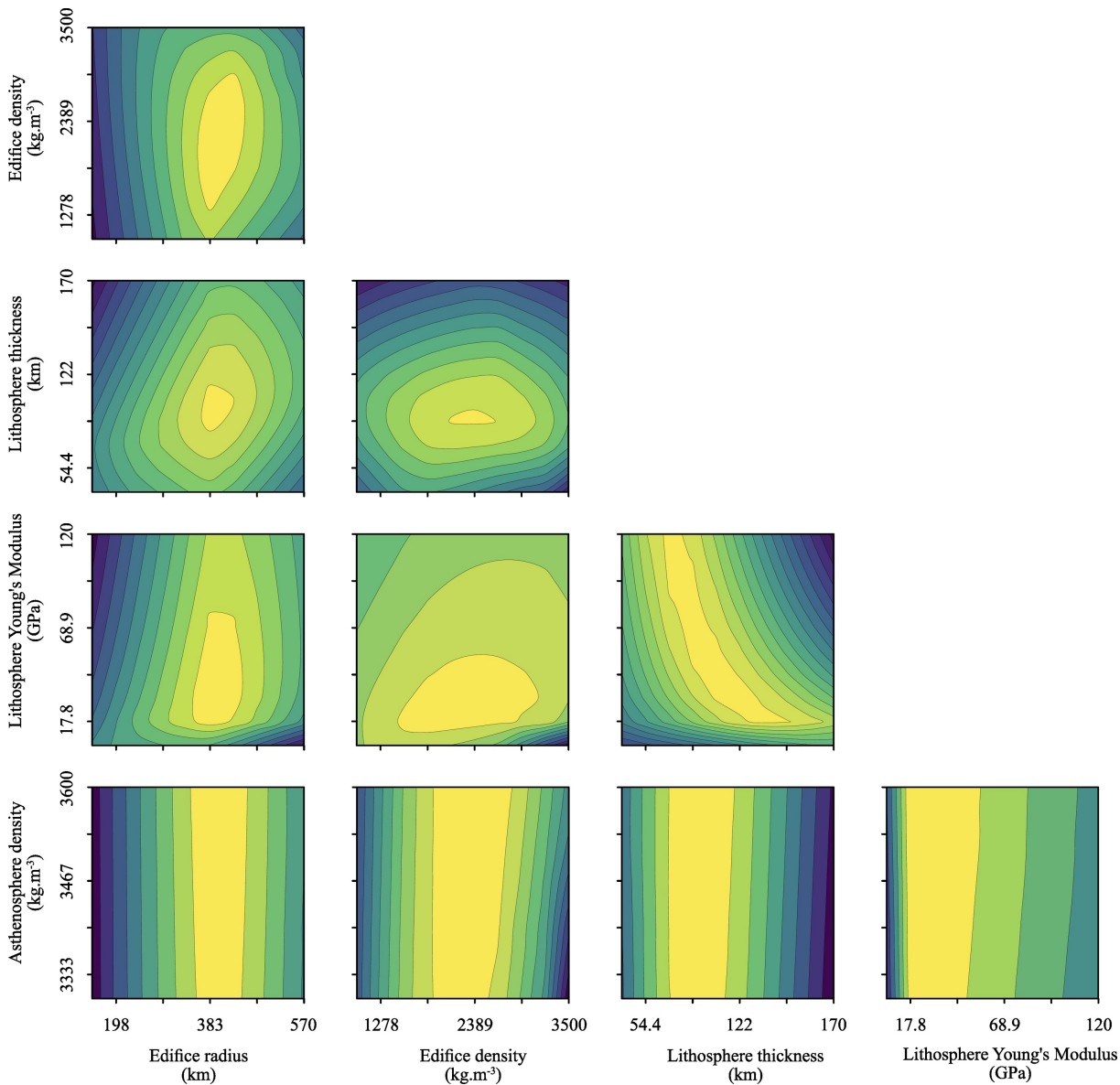


Figure 8